

See discussions, stats, and author profiles for this publication at: <https://www.researchgate.net/publication/237816712>

# Marked Stabilization of Redox States and Enhanced Catalytic Activity in Galactose Oxidase Models Based on Transition Metal S-Methylisothiosemicarbazones with -SR Group in Ortho P...

ARTICLE *in* INORGANIC CHEMISTRY · JUNE 2013

Impact Factor: 4.76 · DOI: 10.1021/ic4004966 · Source: PubMed

---

CITATIONS

8

---

READS

116

## 11 AUTHORS, INCLUDING:



Martin Breza

Slovak University of Technology in Bratislava

164 PUBLICATIONS 835 CITATIONS

[SEE PROFILE](#)



Daniel Végh

Slovak University of Technology in Bratislava

131 PUBLICATIONS 467 CITATIONS

[SEE PROFILE](#)



Joshua Telser

Roosevelt University

150 PUBLICATIONS 9,048 CITATIONS

[SEE PROFILE](#)



Sergiu Shova

Petru Poni Institute of Macromolecular Chemi...

208 PUBLICATIONS 1,675 CITATIONS

[SEE PROFILE](#)

# Marked Stabilization of Redox States and Enhanced Catalytic Activity in Galactose Oxidase Models Based on Transition Metal S-Methylisothiosemicarbazones with –SR Group in Ortho Position to the Phenolic Oxygen

Vladimir B. Arion,\*† Sonja Platzer,† Peter Rapta,\*‡ Peter Machata,‡ Martin Breza,‡ Daniel Végh,‡ Lothar Dunsch,§ Joshua Telser,|| Sergiu Shova,† Tatiana C. O. Mac Leod,# and Armando J. L. Pombeiro\*,#

†Institute of Inorganic Chemistry, University of Vienna, Währinger Strasse 42, A-1090 Vienna, Austria

‡Faculty of Chemical and Food Technology, Slovak University of Technology, Radlinského 9, SK-81237 Bratislava, Slovak Republic

§Centre of Spectroelectrochemistry, Leibniz Institute of Solid State and Materials Research Dresden, Helmholtzstrasse 20, D-01069 Dresden, Germany

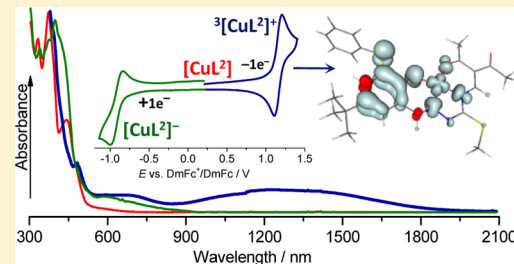
||Department of Biological, Chemical and Physical Sciences, Roosevelt University, 430 South Michigan Avenue, Chicago, Illinois 60605, United States

#“Petru Poni” Institute of Macromolecular Chemistry, Alleea Grigore Ghica Voda 41A, 700487 Iasi, Romania

#Centro de Química Estrutural, Instituto Superior Técnico, Technical University of Lisbon, Lisbon, Portugal

## S Supporting Information

**ABSTRACT:** Reactions of 5-*tert*-butyl-2-hydroxy-3-methylsulfanylbenzaldehyde S-methylisothiosemicarbazone and 5-*tert*-butyl-2-hydroxy-3-phenylsulfanylbenzaldehyde S-methylisothiosemicarbazone with pentane-2,4-dione (Hacac) and triethyl orthoformate in the presence of M(acac)<sub>2</sub> as template source at 107 °C afforded metal complexes of the type M<sup>II</sup>L<sup>1</sup> and M<sup>II</sup>L<sup>2</sup>, where M = Ni and Cu, with a new Schiff base ligand with thiomethyl (H<sub>2</sub>L<sup>1</sup>) and/or thiophenyl (H<sub>2</sub>L<sup>2</sup>) group in the ortho position of the phenolic moiety. Demetalation of NiL<sup>1</sup> in CHCl<sub>3</sub> with HCl(g) afforded H<sub>2</sub>L<sup>1</sup>. The latter reacts with Zn(OAc)<sub>2</sub>·2H<sub>2</sub>O with formation of ZnL<sup>1</sup>. The effect of –SR groups and metal ion identity on stabilization of phenoxy radicals generated electrochemically was studied in detail. A marked stabilization of phenoxy radical was observed in one-electron-oxidized complexes [ML<sup>2</sup>]<sup>+</sup> (M = Ni, Cu) at room temperature, as demonstrated by cyclic voltammetry, EPR spectroscopy, and UV-vis-NIR measurements. In solution, the oxidized CuL<sup>2</sup> and NiL<sup>2</sup> display intense low-energy NIR transitions consistent with their classification as metal-delocalized phenoxy radical species. While the CuL<sup>2</sup> complex shows reversible reduction, reduction of NiL<sup>2</sup>, CuL<sup>1</sup>, and NiL<sup>1</sup> is irreversible. EPR measurements in conjunction with density functional theory calculations provided insights into the extent of electron delocalization as well as spin density in different redox states. The experimental room temperature spectroelectrochemical data can be reliably interpreted with the <sup>3</sup>[CuL<sup>2</sup>]<sup>+</sup> and <sup>2</sup>[NiL<sup>2</sup>]<sup>+</sup> oxidation ground states. The catalytic activity of synthesized complexes in the selective oxidations of alcohols has been studied as well. The remarkable efficiency is evident from the high yields of carbonyl products when employing both the CuL<sup>2</sup>/air/TEMPO and the CuL<sup>2</sup>/TBHP/MW(microwave-assisted) oxidation systems.



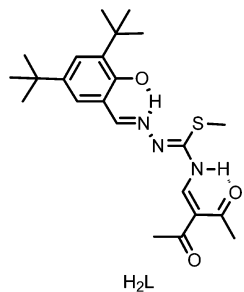
## INTRODUCTION

Quite recently, we reported the template synthesis of a new ligand with a N<sub>2</sub>O<sub>2</sub> donor set with a single phenolic moiety, suitably protected by bulky *tert*-butyl groups in the 3,5-positions of the parent phenol able to generate a phenoxy radical, and which contains a thiomethyl group attached to the extended π-conjugated ligand backbone (Scheme 1).<sup>1</sup> This tetradeятate ligand proved to be suitable for the synthesis of metal complexes (e.g., Ni, Cu, Zn) as models for mimicking the electronic structure and reproducing some spectroscopic features of galactose oxidase (GO) and glyoxal oxidase

(GLO).<sup>2–6</sup> The active site of these two enzymes involves copper(II) bound by a thioether-modified tyrosyl radical. The metalloenzymes catalyze the two-electron oxidation of primary alcohols to aldehydes and oxidation of aldehydes to carboxylic acids, with concomitant reduction of O<sub>2</sub> to H<sub>2</sub>O<sub>2</sub>. One-electron electrochemical oxidation of the ligand H<sub>2</sub>L gave rise to a cation radical H<sub>2</sub>L<sup>•+</sup>, which was not stable, but detectable at room temperature by EPR spectroscopy. A marked stabilization of

Received: February 26, 2013

Published: June 12, 2013

**Scheme 1.** Structure of the Tetridentate  $N_2O_2$  Ligand  $H_2L$ 

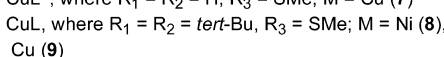
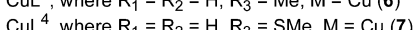
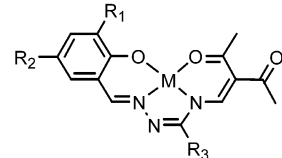
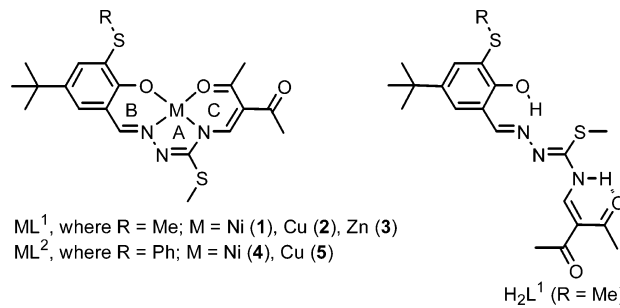
phenoxyl radical was observed in one-electron-oxidized complexes  $[ML]^{+}$  at room temperature, as demonstrated by cyclic voltammetry, EPR spectroscopy, and UV-vis-NIR measurements. This stabilization occurred with no contribution from the metal ion in the case of redox inactive  $Zn^{II}$  or with some contribution from the d-orbitals of redox-active metal ions ( $Ni^{II}$ ,  $Cu^{II}$ ).

Concurrent results reported by others showed<sup>7</sup> that a large cathodic shift in the redox potential was observed for a  $Cu^{II}$  model compound with a thiomethyl group in the ortho position of the phenol ring as compared to an unsubstituted phenol derivative, and that such complexes have spectroscopic characteristics closer to those of GO.<sup>8,9</sup> The shift was attributed to both the electron-donating nature of the thiomethyl group and its radical stabilizing effect by electron spin-delocalization (i.e., an electron-sharing conjugative effect). In contrast, our experimental data and density functional theory (DFT) calculations suggested a lack of electron-spin delocalization into the remote  $SCH_3$  group in  $H_2L$ . The question whether replacement of the *tert*-butyl group in the ortho position of the phenolic moiety by a thiomethyl or thioaryl group can produce a better model of GO/GLO remained to be clarified. A large number of phenolate and bis(phenolate) copper(II) complexes, which can reproduce the spectroscopic properties and/or reactivity of these metalloenzymes, have been documented in the literature.<sup>10–15</sup>

Herein we report on the synthesis of five new nickel(II), copper(II), and zinc(II) complexes  $ML^1$  and  $ML^2$  (Scheme 2) with tetridentate  $N_2O_2$  ligands closely related to  $H_2L$ , in which the *tert*-butyl group in the ortho position of the phenolic moiety was replaced respectively by thiomethyl ( $H_2L^1$ ) and thiophenyl ( $H_2L^2$ ) groups.

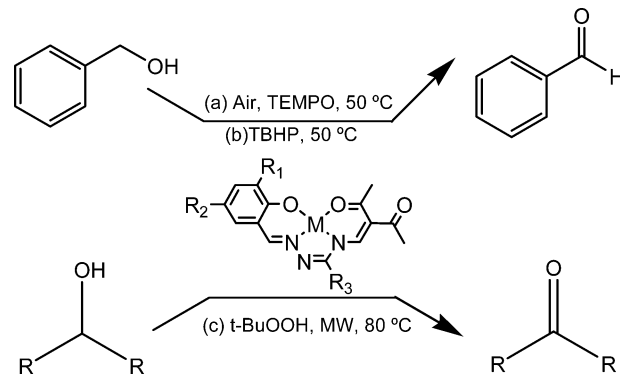
The effect of these groups and of metal ion identity on stabilization of the one-electron-oxidized species generated electrochemically, as well as characterization of their electronic structures by various spectroscopic methods and DFT calculations, is explored in this work. In addition, the catalytic activity of the  $ML^1$  and  $ML^2$  complexes (structures 1–5 in Scheme 2) in homogeneous oxidation of primary and secondary alcohols has been assayed and compared to those of previously synthesized and characterized copper(II) complexes (structures 6 and 7 in Scheme 2)<sup>16,17</sup> as well as nickel(II) and copper(II) ML complexes protected by bulky *tert*-butyl groups in the 3,5-positions of the parent phenol (structures 8 and 9 in Scheme 2).<sup>1</sup>

The use of these complexes with tetridentate  $N_2O_2$  ligands as catalysts (or catalyst precursors) for the oxidation of alcohols to the corresponding carbonyl products was applied to primary (benzyl alcohol) and secondary (1-phenylethanol) alcohols by exploring two different oxidants: TBHP (*tert*-butyl hydro-

**Scheme 2.** Structures of Compounds Synthesized and Investigated in the Present Study<sup>a</sup>

<sup>a</sup>Compounds 1–5 and  $H_2L^1$  have been prepared in this work, while 6–9 were reported previously.

peroxide) and air/TEMPO (TEMPO = 2,2,6,6-tetramethylpiperidine-1-oxyl), as illustrated in Scheme 3a,b. The studied

**Scheme 3.** (a) Aerobic TEMPO-Mediated Oxidation of Benzyl Alcohol, (b) Peroxidative Oxidation of Benzyl Alcohol Using TBHP, and (c) Solvent-Free Peroxidative Oxidation of Secondary Alcohols under Microwave (MW) Irradiation

TEMPO-mediated aerobic oxidation with copper(II) S-methylisothiosemicarbazone complexes as catalyst conceivably involves a similar pathway to that previously proposed for other Cu/air/TEMPO systems of the galactose oxidase type.<sup>18</sup> The first steps of the catalytic cycle are similar to those proposed for GO: alcohol is coordinated to the copper center, followed by the Cu-centered oxidative dehydrogenation of alcohol via H-atom abstraction and one-electron oxidation while  $Cu^{II}$  is reduced to  $Cu^I$ . The initial  $Cu^{II}$  complex is regenerated by the TEMPO-mediated oxidation of  $Cu^I$  to  $Cu^{II}$ , whereas TEMPO is regenerated by the aerobic oxidation of TEMPOH.<sup>19</sup> Finally, we have tested also the strategy recently developed by some of us based on microwave-assisted oxidation of secondary alcohols in a solvent-free system using TBHP as oxidant (Scheme 3c).<sup>20</sup>

## RESULTS

**Synthesis.** Template condensation of 5-*tert*-butyl-2-hydroxy-3-methylsulfanylbenzaldehyde *S*-methylisothiocarbazole with pentane-2,4-dione and triethyl orthoformate in the presence of  $M(acac)_2$  at 107 °C afforded metal complexes of the type  $M^{II}L^1$ , where  $M = Ni$  and  $Cu$ , and  $H_2L^1 = 9-(2'-hydroxy-3'-methylthio-5'-*tert*-butylphenyl)-6-methylthio-3-acetyl-5,7,8-triazanona-3,6,8-trien-2-one$  (Scheme 2).

Analogously starting from 5-*tert*-butyl-2-hydroxy-3-phenylsulfanylbenzaldehyde, *S*-methylisothiocarbazole complexes  $M^{II}L^2$  ( $M = Ni, Cu$ ) were prepared. Evidence for the formation of metal complexes with new tetradentate ligands  $H_2L^1$  and  $H_2L^2$  was furnished by the positive ESI mass spectra, which showed the presence of peaks with  $m/z$  478, 500, 516 and 483, 505, 521 for  $NiL^1$  and  $CuL^1$ , respectively, due to the formation of ions  $[ML^1 + H]^+$ ,  $[ML^1 + Na]^+$ ,  $[ML^1 + K]^+$ , and with  $m/z$  540, 562 and 545, 567 for  $NiL^2$  and  $CuL^2$ , respectively, due to formation of ions  $[ML^2 + H]^+$ ,  $[ML^2 + Na]^+$ . By using the same synthetic procedure, a number of metal complexes with related tetradentate ligands have been prepared and reported previously.<sup>17,21–23</sup> The reaction does not work in the absence of metal ions. It should, however, be noted that the synthesis of a metal-free tetradentate Schiff base with unsubstituted phenolic moiety was performed in the presence of  $VO^{2+}$  and  $Zn^{2+}$ , making use of their catalytic coordination template effect.<sup>17,24</sup> Demetalation of  $NiL^1$  with gaseous hydrogen chloride in chloroform afforded the metal-free ligand  $H_2L^1$ . This showed in the mass spectrum peaks at  $m/z$  422, 444, and 460 attributable to  $[L^1 + H]^+$ ,  $[L^1 + Na]^+$ , and  $[L^1 + K]^+$ , respectively. By reaction of  $H_2L^1$  with  $Zn(OAc)_2 \cdot 2H_2O$  in a 1:1 molar ratio in methanol, the complex  $ZnL^1$  was isolated. The ESI mass spectrum consisted of three peaks with  $m/z$  486, 506, and 522, which can be attributed to  $[ZnL^1 + H]^+$ ,  $[ZnL^1 + Na]^+$ , and  $[ZnL^1 + K]^+$ , respectively.

**X-ray Crystallography.** The results of X-ray diffraction studies of  $NiL^1$ ,  $CuL^1$ ,  $ZnL^1$ ,  $H_2L^1$ , and  $NiL^2$  are shown in Figures 1 and 2, correspondingly. Selected bond distances (Å) and angles (deg) are quoted in Table 1. The metal ion is coordinated by two nitrogen atoms (N1, N3) and two oxygen atoms (O1, O2). The coordination geometry about nickel(II) and copper(II) can be described as square-planar. The coordinated atoms O1, O2, N1, and N3 are almost coplanar with deviations from the mean planes within  $\pm 0.042$ ,  $\pm 0.022$ , and  $\pm 0.019$  Å for  $NiL^1$ ,  $CuL^1$ , and  $NiL^2$ , respectively. The dihedral angle between the two O–M–N planes in  $NiL^1$  and  $CuL^1$  is at 176.2 and 177.7°, correspondingly, while in  $NiL^2$  it is at 178.0°. The coordination polyhedron of zinc(II) in  $ZnL^1(O1^i)$  [symmetry code used: (i)  $-x + 1, -y + 1, -z$ ] is a square-pyramid ( $\tau = 0.05$ ).<sup>25</sup> The apical coordination site is occupied by an oxygen atom  $O1^i$  of the neighboring molecule of the complex with  $Zn–O1^i$  bond at 2.073(4) Å. The coordinated atoms O1, O2, N1, and N3 in the basal plane of the pyramid in  $ZnL^1(O1^i)$  deviate from their least-squares mean plane within  $\pm 0.021$  Å. The zinc(II) ion comes out from this plane by 0.364 Å toward the apical ligand. Unlike in  $NiL^1$  and  $CuL^1$ , the coordinated ligand ( $L^1$ )<sup>2-</sup> in  $ZnL^1$  is markedly distorted from planarity. The dihedral angle between the two O–Zn–N planes in  $ZnL^1(O1^i)$  is at 151.0°. Two  $ZnL^1$  molecules form a centrosymmetric dimer via intermolecular apical interactions  $Zn–O1^i$  and  $Zn<sup>i</sup>–O1$  with  $Zn\cdots Zn^i$  separation of 2.9927(14) Å (Figure 2). Similar arrangement of two neutral molecules in a dimer showing the  $Zn_2O_2$  core

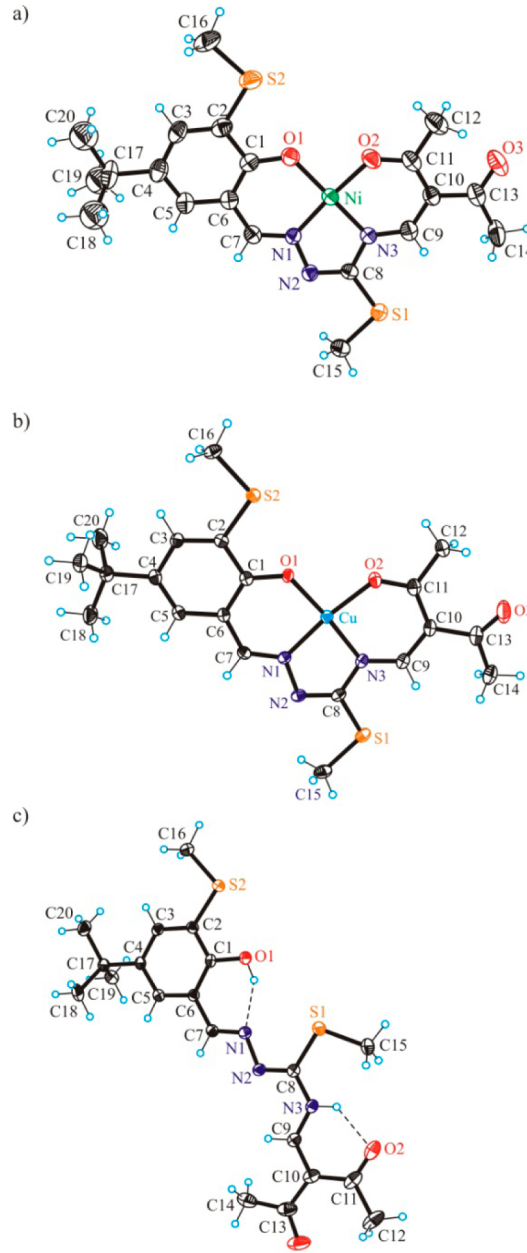
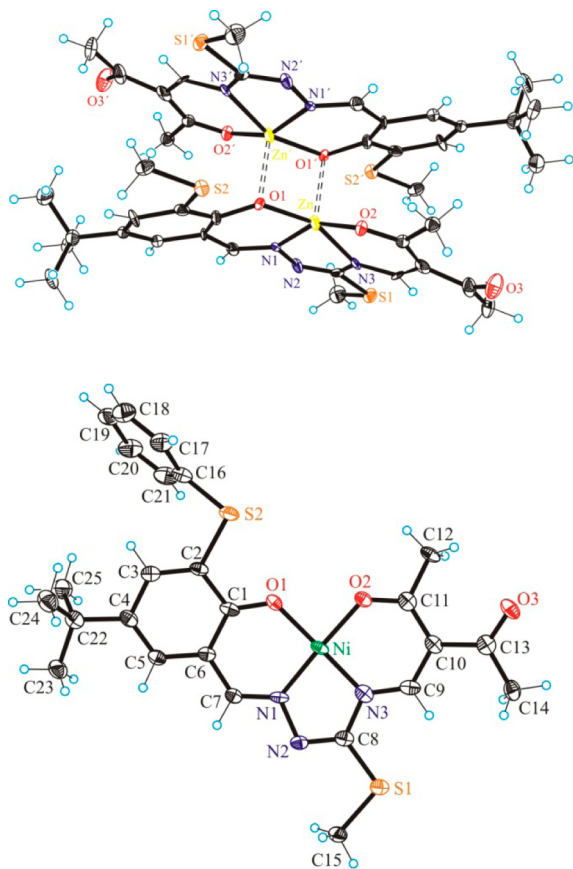


Figure 1. ORTEP views of (a)  $NiL^1$ , (b)  $CuL^1$ , and (c)  $H_2L^1$  with atom labeling and thermal ellipsoids at the 50% probability level.

was reported for  $[Zn(Salpr)]_2$  (where Salpr = *N,N'*-bis(salicylidene)-1,3-propanediamine).<sup>26</sup> Trigonal-bipyramidal geometry of central ions was found in a centrosymmetric di- $\mu$ -phenoxido bridged zinc dimer  $[SalomphanH_2Zn]_2$ , where Salomphan = *N,N'*-(4,5-dimethyl)phenylbis(*o*-hydroxybenzylamine), a more flexible ligand compared to  $H_2L^1$ ,<sup>27</sup> while in  $Zn_2(H_2SB)_2 \cdot 3H_2O \cdot Me_2CO$ , where  $H_4SB = N,N'$ -bis(2,5-dihydroxybenzylidene)-1,4-diaminobutane, the coordination geometry of Zn1 is better described as square-pyramidal ( $\tau = 0.43$ ) and that of Zn2 as trigonal bipyramidal ( $\tau = 0.61$ ).<sup>28</sup>

The configurations adopted by the ligand  $H_2L^1$  in metal complexes and in the metal-free state are quite different. The ligand is in *Z* configuration with respect to the central N2=C8 bond in  $NiL^1$ ,  $CuL^1$  and  $[ZnL^1]_2$ , while it is in the *E* configuration in  $H_2L^1$ . For metal coordination to occur, two rotations of the relevant moieties in the metal-free ligand are



**Figure 2.** ORTEP view of  $[ZnL^1]_2$  (top) with labeling of noncarbon atoms and  $NiL^2$  (bottom) with labeling of nonhydrogen atoms and thermal ellipsoids at the 50% probability level. Selected bond distances ( $\text{\AA}$ ) and bond angles (deg): Ni–O1 1.824(4), Ni–O2 1.852(4), Ni–N1 1.822(4), Ni–N3 1.818(5), C7–N1 1.297(7), N1–N2 1.408(6), N2–C8 1.284(7), C8–N3 1.406(7), N3–C9 1.307(7), C9–C10 1.399(8), C10–C11 1.428(8), C11–O2 1.253(7); O1–Ni–N1 95.38(19), N1–Ni–N3 83.8(2), N3–Ni–O2 93.60(19), O1–Ni–O2 87.25(17).

**Table 1. Selected Bond Distances ( $\text{\AA}$ ) and Bond Angles (deg) in  $ML^1$  ( $M = \text{Ni}, \text{Cu}, \text{Zn}$ ) and  $H_2L^1$**

	$NiL^1$	$CuL^1$	$ZnL^1$	$H_2L^1$
M–O1	1.829(4)	1.8792(15)	1.995(4)	
M–O2	1.855(4)	1.9185(17)	2.021(4)	
M–N1	1.822(5)	1.916(2)	2.040(5)	
M–N3	1.824(4)	1.914(2)	2.015(5)	
C6–C7	1.417(8)	1.425(3)	1.449(8)	1.448(2)
C7–N1	1.311(7)	1.295(3)	1.291(8)	1.287(2)
N1–N2	1.398(6)	1.401(3)	1.391(7)	1.392(2)
N2–C8	1.295(7)	1.303(3)	1.306(8)	1.291(2)
C8–N3	1.397(7)	1.393(3)	1.370(8)	1.384(2)
N3–C9	1.322(7)	1.329(3)	1.329(8)	1.343(2)
C9–C10	1.389(8)	1.392(4)	1.403(9)	1.377(3)
C10–C11	1.426(9)	1.447(4)	1.436(9)	1.471(3)
C11–O2	1.262(7)	1.265(3)	1.258(7)	1.233(3)
O1–M–N1	95.57(18)	94.25(8)	89.54(18)	
N1–M–N3	83.58(19)	81.43(8)	77.02(19)	
O1–M–O2	87.83(18)	92.95(7)	99.04(17)	
N3–M–O2	93.14(19)	91.38(8)	86.87(19)	

required, one around the  $\text{N}2=\text{C}8$  bond and the second around the  $\text{N}3–\text{C}8$  bond.

The doubly deprotonated tetradentate ligands ( $L^1$ )<sup>2-</sup> and ( $L^2$ )<sup>2-</sup> form three metallocycles upon coordination to the metal, one five-membered A and two six-membered B and C (see Scheme 2). The M–O1, M–O2, M–N1, and M–N3 distances in  $NiL^1$  and  $CuL^1$  (Table 1) are comparable to those in  $NiL$ ,  $NiL^2$  (see Table 1 and legend to Figure 2) and other related compounds.<sup>21–23</sup> Less geometrical similarity is observed for Zn–O1, Zn–O2, Zn–N1, and Zn–N3 distances in  $ZnL^1(O1^i)$  (Table 1) and in square-pyramidal complex  $ZnL\cdot\text{MeOH}$ .<sup>1</sup>

Strong  $\pi$ -delocalization is evident in both the fragment C6–C7–N1–N2–C8–N3 and the pentane-2,4-dione moiety of  $NiL^1$  and  $CuL^1$ , while it is less pronounced in  $ZnL^1(O1^i)$  and not obvious in  $H_2L^1$  (see Table 1).

The  $E$  configuration adopted by the molecule of  $H_2L^1$  is not strictly planar. The dihedral angle between the mean plane through the isothiosemicarbazide moiety and phenolic ring is 2.4°, while that between the isothiosemicarbazide fragment and flat acetylacetone moiety is at 5.1°.

**Cyclic Voltammetry.** The cyclic voltammograms of  $NiL^1$ ,  $CuL^1$ , and  $H_2L^1$  in  $\text{CH}_2\text{Cl}_2$  containing 0.1 M TBAPF<sub>6</sub> as the supporting electrolyte using a platinum wire working electrode are shown in Figure 3a, while oxidation and reduction peak potentials as well as half-wave potentials are given in Table 2.

The redox potentials are quoted against the decamethylferrocenium/decamethylferrocene couple (DmFc<sup>+</sup>/DmFc). The  $E_{1/2}(\text{Fc}^+/\text{Fc}) - E_{1/2}(\text{DmFc}^+/\text{DmFc})$  value of 0.54 V obtained in an independent experiment can be used to recalculate the sample oxidation potentials vs the Fc<sup>+</sup>/Fc couple.

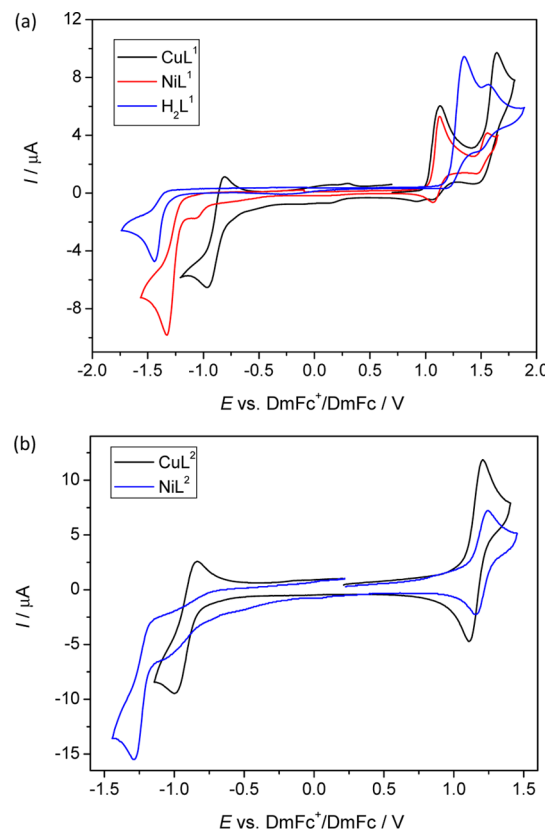


**Figure 3.** (a) Comparison of cyclic voltammograms of  $H_2L^1$ ,  $NiL^1$ , and  $CuL^1$  in  $\text{CH}_2\text{Cl}_2$ . (b) Comparison of cyclic voltammograms of  $NiL^2$  and  $CuL^2$  in  $\text{CH}_2\text{Cl}_2$  (room temperature, 0.10 M TBAPF<sub>6</sub>, scan rate 100 mV s<sup>-1</sup>, platinum wire working electrode).

**Table 2. Comparison of Redox Potentials ( $E_{\text{pa}}$  – Anodic Peak Potential,  $E_{\text{pc}}$  – Cathodic Peak Potential,  $E_{1/2}$  – Half-Wave Potential) Against DmFc<sup>+</sup>/DmFc for Oxidation and Reduction of NiL<sup>1</sup>, CuL<sup>1</sup>, H<sub>2</sub>L<sup>1</sup>, NiL<sup>2</sup>, and CuL<sup>2a</sup>**

	$E^{\text{red}}/\text{V}$			$E^{\text{ox}}/\text{V}$			follow-up product		
	$E_{\text{pc}}$	$E_{\text{pa}}$	$E_{1/2}$	1st step			$E_{\text{pa}}$	$E_{\text{pc}}$	$E_{1/2}$
				$E_{\text{pa}}$	$E_{\text{pc}}$	$E_{1/2}$			
NiL <sup>1</sup>	–1.32			1.13			1.56	1.45	1.51
CuL <sup>1</sup>	–0.94	–0.82	–0.88	1.10			1.63	1.46	1.54
H <sub>2</sub> L <sup>1</sup>	–1.43			1.34			1.58	1.48	1.53
NiL <sup>2</sup>	–1.29			1.23	1.14	1.19	1.92		
CuL <sup>2</sup>	–1.02	–0.85	–0.94	1.21	1.12	1.16	1.86		

<sup>a</sup> $E_{1/2}(\text{Fc}^+/\text{Fc}) - E_{1/2}(\text{DmFc}^+/\text{DmFc}) = 0.54 \text{ V}$ .

The electrochemical properties of all three compounds are comparable. Upon oxidation of CuL<sup>1</sup>, an irreversible anodic peak at  $E_{\text{pa}}$  1.10 V was observed with a small cathodic peak when potential is reversed, which decreases by decreasing the scan rate (Figure S1a in the Supporting Information), indicating follow-up reactions of primarily formed oxidized species. At a scan rate of 5 mV s<sup>–1</sup> the first oxidation is already irreversible. The behavior of NiL<sup>1</sup> is similar (see red trace in Figure 3a) with the first nearly irreversible voltammetric peak at 1.13 V, but the corresponding cathodic peak, when potential is reversed, is more visible. A second oxidation peak arises at slightly lower oxidation potential compared to that for CuL<sup>1</sup>. The current height is, however, considerably less compared to the first one. This indicates that this peak corresponds to the oxidation of the follow-up product. In the case of H<sub>2</sub>L<sup>1</sup> the first oxidation wave is fully irreversible and exhibits the highest anodic peak potential at  $E_{\text{pa}} = 1.34 \text{ V}$  vs DmFc<sup>+</sup>/DmFc. The second much smaller oxidation peak attributed to the oxidation of the follow-up product exhibits a quasireversible behavior with  $E_{1/2}$  1.53 V. A marked cathodic shift in the redox potential from  $E_{1/2}$  0.67 V to  $E_{1/2}$  0.55 V and from  $E_{1/2}$  0.62 V to  $E_{1/2}$  0.53 V vs Fc<sup>+</sup>/Fc couple occurs on passing from NiL to NiL<sup>1</sup>, and from CuL to CuL<sup>1</sup>, respectively.<sup>1</sup> This shift is due to replacement of the *tert*-butyl group in ortho position of the phenolic oxygen in H<sub>2</sub>L (Scheme 1) by the electron-donating thiomethyl group.

In the cathodic part the redox couple at –0.88 V corresponds to a reduction of CuL<sup>1</sup> yielding the reduced complex [CuL<sup>1</sup>]<sup>–</sup>. This process is more reversible compared to the first oxidation wave, indicating increased stability of the one-electron-reduced species in comparison to one-electron-oxidized species. The reduction wave of CuL<sup>1</sup> becomes irreversible at scan rates up to 5 mV s<sup>–1</sup>. Reduction of H<sub>2</sub>L<sup>1</sup> and NiL<sup>1</sup> at higher scan rates (up to 100 mV s<sup>–1</sup>) is irreversible. Overall the separation between the first oxidation and reduction processes is the smallest for CuL<sup>1</sup>, followed by NiL<sup>1</sup> and H<sub>2</sub>L<sup>1</sup>, indicating that CuL<sup>1</sup> is easiest both to oxidize and to reduce, although it should be noted that the redox potentials determined for NiL<sup>1</sup> and CuL<sup>1</sup> are very similar.

In contrast to CuL<sup>1</sup>, upon oxidation of CuL<sup>2</sup>, where (L<sup>2</sup>)<sup>2–</sup> is a tetradentate ligand with –SPh group in ortho position to phenolic oxygen, a fully reversible redox couple was observed for the first electron transfer. In Figure 3b cyclic voltammograms of CuL<sup>2</sup> and NiL<sup>2</sup> are shown for comparison. This process is reversible in the whole range of scan rates applied from 5 to 100 mV s<sup>–1</sup> for CuL<sup>2</sup> (Figure S1b in the Supporting Information). The second oxidation peak for CuL<sup>2</sup> (not shown) is irreversible and indicates complex redox behavior at higher anodic potentials. As for CuL<sup>1</sup> and NiL<sup>1</sup>, CuL<sup>2</sup> is both

more easily oxidized and reduced than NiL<sup>2</sup>. Reduction of CuL<sup>2</sup> is less reversible compared to its oxidation. Compared to one-electron reduction of CuL<sup>1</sup> the reduction of CuL<sup>2</sup> is less reversible. The anodic behavior of NiL<sup>2</sup> is similar to that for CuL<sup>2</sup> (Figure 3b) with the first reversible oxidation seen even at a scan rate of 5 mV s<sup>–1</sup>. The cathodic behavior of NiL<sup>2</sup> differs significantly from that for CuL<sup>2</sup>. While the copper(II) complex shows reversible reduction, reduction of the nickel(II) complex is irreversible as already mentioned for CuL<sup>1</sup> and NiL<sup>1</sup>.

Cyclic voltammetry studies suggest that one can expect the formation of stable phenoxyl radical species in the region of the first anodic peak for NiL<sup>2</sup> and CuL<sup>2</sup>. The half-wave potentials of NiL<sup>2</sup> and CuL<sup>2</sup> are very similar, and consequently a ligand-centered oxidation seems most likely. In contrast, the first cathodic half-wave potentials of NiL<sup>2</sup> (–1.29 V) and CuL<sup>2</sup> (–1.02 V) differ considerably and can therefore be assigned to a metal-centered reduction. The first cathodic peak observed for CuL<sup>2</sup> is probably due to the reversible reduction of Cu<sup>II</sup>L<sup>2</sup> to Cu<sup>I</sup>L<sup>2</sup>. Nearly the same potentials for anodic processes and irreversible first anodic voltammetric peaks observed for NiL<sup>1</sup> and CuL<sup>1</sup> indicate ligand based oxidation under formation of unstable phenoxyl radical species. However, the presence of the corresponding cathodic peak when the potential is reversed for NiL<sup>1</sup> suggests that this radical might be detectable by EPR spectroscopy as will be discussed in more detail in the following section.

**EPR and UV–Vis–NIR Spectroelectrochemistry.** Cyclic voltammograms and simultaneously recorded evolution of UV–vis spectra for NiL<sup>1</sup> provide further evidence for irreversibility of the redox processes (Figures S2 and S3 in the Supporting Information). The detection of the emerging radical upon oxidation was possible only by using a freshly prepared and well-dried supporting electrolyte (Figure S2c in the Supporting Information). This radical species showed a very short lifetime (less than 1 s). Evolution of UV–vis spectra upon reduction of NiL<sup>1</sup> in CH<sub>2</sub>Cl<sub>2</sub> (Figure S3 in the Supporting Information) is similar to that observed upon oxidation. No EPR signal was registered upon reduction, indicating very unstable paramagnetic intermediates, if formed at all.

On the other hand, upon oxidation of NiL<sup>2</sup> a nearly reversible redox couple in the corresponding cyclic voltammogram at 5 mV s<sup>–1</sup> was observed (Figure 4a). A new NIR absorption band with a maximum at 1235 nm was registered in the region of the first oxidation peak (Figure 4b). Simultaneously, a new, single line EPR spectrum was observed with g value = 2.0092 and a line width p.p. = 4.7 G (Figure 4c). This EPR line, with g value higher than that typical for organic radicals, indicates that this signal can be assigned to a species of

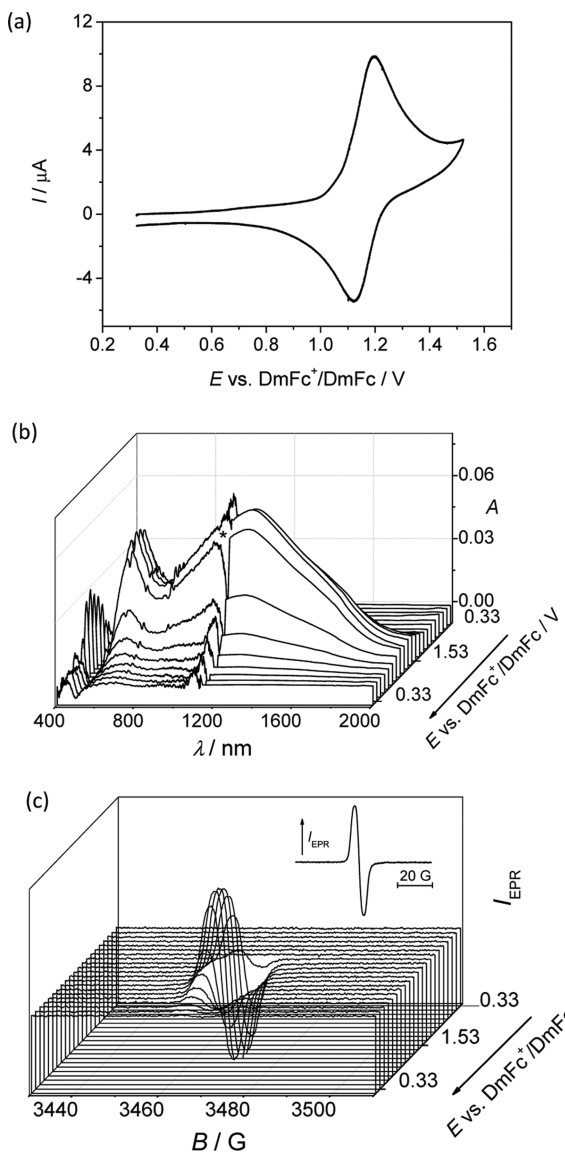


**Figure 4.** Spectroelectrochemistry of  $\text{NiL}^2$  oxidation in  $\text{CH}_2\text{Cl}_2$  (0.2 M TBAPF<sub>6</sub>, platinum wire working electrode): (a) Cyclic voltammetry at scan rate of  $5 \text{ mV s}^{-1}$  and corresponding in situ potential dependence of (b) vis–NIR (\* artifact from equipment) and (c) EPR spectra of  $[\text{NiL}^2]^+$ .

predominantly phenoxyl radical character, but with a marked contribution from the Ni(II) atom (this  $g > 2.00$  results from the contribution of Ni(II) with its more than half-filled  $3d^8$  configuration). Upon reduction, there was no EPR signal observed and negligible changes in UV–vis spectra were found.

For CuL<sup>2</sup>, reversible one-electron oxidation was observed in situ in acetonitrile or  $\text{CH}_2\text{Cl}_2$  upon cyclic voltammetry at  $5 \text{ mV s}^{-1}$  at the first oxidation peak ( $E_{1/2} 1.16 \text{ V}$ ) with simultaneous increase of new optical absorption bands at 678, 1217, and 1430 nm as illustrated in Figure 5. A slight decrease of the well-defined four component room temperature EPR signal (due to the nuclear spin  $I = 3/2$  for  $^{63,65}\text{Cu}$ , see inset in Figure 5a) was observed simultaneously. The EPR spectrum of CuL<sup>2</sup> initial solution in  $\text{CH}_2\text{Cl}_2/\text{DMF}$  (1:1) at 100 K exhibits a characteristic axial symmetry pattern (Figure S4a in the Supporting Information). A marked decrease of Cu<sup>II</sup> EPR signal at the first oxidation peak was confirmed using a large Pt mesh (Figure S4b in the Supporting Information).

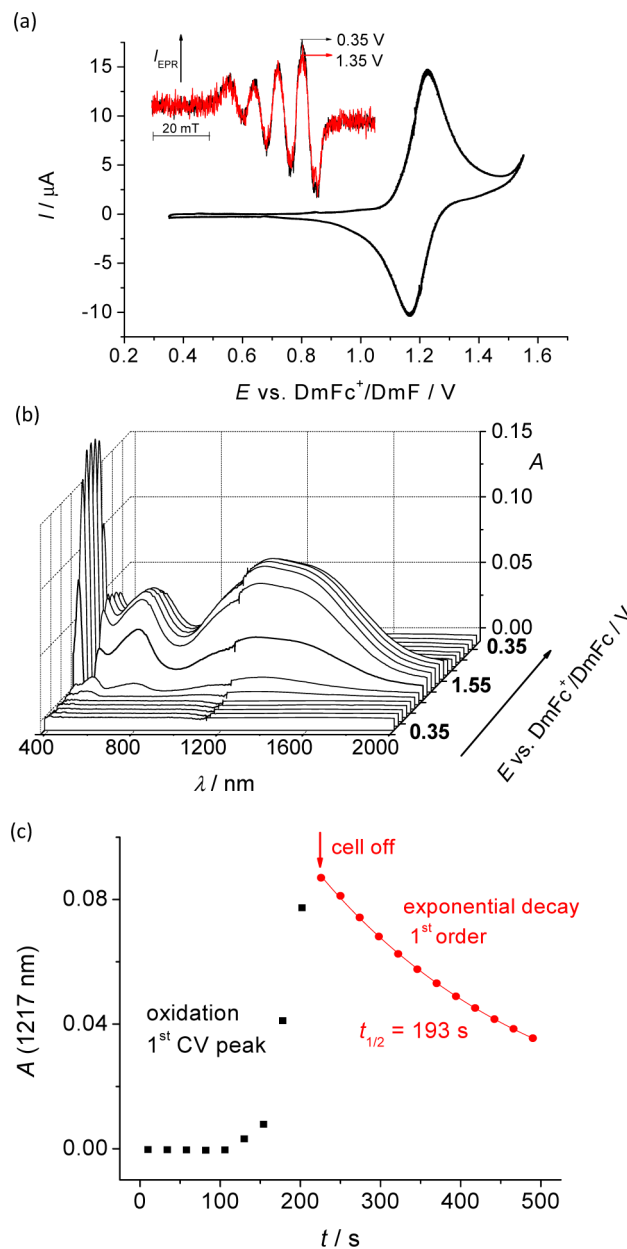


**Figure 5.** Spectroelectrochemistry of  $\text{CuL}^2$  in acetonitrile: (a) Cyclic voltammetry (0.1 M TBAPF<sub>6</sub>, scan rate  $5 \text{ mV s}^{-1}$ , platinum mesh working electrode) and (b) corresponding potential dependence of vis–NIR spectra. (c) Measurement of lifetime of phenoxyl radical in  $[\text{CuL}^2]^+$  using vis–NIR spectroelectrochemistry. Inset in panel a: EPR spectra measured in situ during cyclic voltammetry of  $\text{CuL}^2$  at 0.35 V and at 1.35 V (behind CV peak maximum) vs DmFc<sup>+</sup>/DmFc using small laminated Pt mesh electrode.

The lifetime of the oxidized CuL<sup>2</sup> was determined to be about 300 s, confirming the marked stabilization effect of the –SPh group. This lifetime was determined as follows. Cyclic voltammetry at the first oxidation wave was stopped when the maximal intensity of NIR band at 1217 nm ( $\epsilon = 6700 \text{ M}^{-1} \text{ cm}^{-1}$ ) was achieved. At this point, the decrease of this absorbance was monitored (Figure 5c). This decay was found to be a first-order process with a half-life of 193 s at 23 °C ( $k_{\text{obs}} = 3.60 \times 10^{-3} \text{ s}^{-1}$ ). Note that this radical is not observable directly by EPR spectroscopy because of spin coupling of the paramagnetic Cu<sup>II</sup> ( $S = 1/2$ ) with the phenoxyl radical moiety of the ligand ( $S = 1/2$ ) as discussed in more detail below.

Copper(II)–phenoxy radical species are known to undergo magnetic exchange interactions between Cu<sup>II</sup> and the phenoxy radical.<sup>29–38</sup>

Results from the spectroelectrochemistry of one-electron reduction of CuL<sup>2</sup> are shown in Figure S5 in the Supporting Information. A new dominating band at 420 nm arises upon reduction along with a new low intensity band at 650 nm. In comparison to oxidation, this reduction process is less reversible, as already shown by cyclic voltammetry of this compound.

**DFT Calculations.** DFT calculations of M<sup>II</sup>L<sup>1</sup> (M = Ni, Cu) and NiL<sup>2</sup> well reproduce the geometrical parameters of the corresponding complexes established by X-ray diffraction. At the B3LYP/6-311G\* level of theory, geometry optimization yields calculated bond distances of the coordination spheres in good agreement with those from X-ray diffraction (within  $\pm 0.032$  Å; see Tables 1 and 3). Based on these results, the

**Table 3. Metal–Ligand Bond Lengths,  $d(M-X)$  [Å], Obtained by DFT Geometry Optimization**

	M–O1	M–O2	M–N1	M–N3
$^2[CuL^1]^0$	1.892	1.934	1.924	1.944
$^1[CuL^1]^+$	1.861	1.878	1.907	1.891
$^3[CuL^1]^+$	1.945	1.902	1.945	1.919
$^1[NiL^1]^0$	1.837	1.856	1.833	1.850
$^3[NiL^1]^0$	1.875	1.965	1.956	1.965
$^2[NiL^1]^+$	1.860	1.838	1.847	1.835
$^2[CuL^2]^0$	1.892	1.935	1.925	1.944
$^1[CuL^2]^+$	1.946	1.902	1.945	1.919
$^3[CuL^2]^+$	1.944	1.903	1.944	1.919
$^1[NiL^2]^0$	1.837	1.856	1.833	1.850
$^3[NiL^2]^0$	1.876	1.965	1.955	1.964
$^2[NiL^2]^+$	1.858	1.839	1.846	1.835

geometries of one-electron-oxidized species [ML<sup>1</sup>]<sup>+</sup> and [ML<sup>2</sup>]<sup>+</sup> in the singlet, doublet, and/or triplet ground state(s) have been also optimized. A contraction in bond lengths of the coordination sphere by 0.02–0.06 Å is observed upon going from  $^2[CuL^1]^0$  to  $^1[CuL^1]^+$ . Unlike, on going from  $^2[CuL^2]^0$  to  $^1[CuL^2]^+$ , a shortening of Cu–O2 and Cu–N3 bonds by 0.03 Å and lengthening of Cu–O1 and Cu–N1 by 0.02 to 0.05 Å is observed. Similar tendencies are seen upon going from  $^1[NiL^1]^0$  to  $^2[NiL^1]^+$  and from  $^1[NiL^2]^0$  to  $^2[NiL^2]^+$ .

Time-dependent DFT (TD-DFT) calculations predict correctly the absence of intense transitions for ML<sup>1</sup> and ML<sup>2</sup> at energies lower than 18000 cm<sup>-1</sup> and the existence of two low-energy transitions for one-electron-oxidized species. In Figure 6, experimental electronic absorption spectra for CuL<sup>2</sup> and those for [CuL<sup>2</sup>]<sup>+</sup>, generated electrochemically by one-electron oxidation of CuL<sup>2</sup>, were compared with theoretical electronic transitions calculated for  $^2[CuL^2]^0$  (Figure 6a) and [CuL<sup>2</sup>]<sup>+</sup> in the singlet and triplet states (Figure 6b).

For  $^2[CuL^2]$ , the first transition with significant oscillator strength corresponds mainly to that from  $\alpha$ -HOMO to  $\alpha$ -LUMO and from  $\beta$ -HOMO to  $\beta$ -LUMO+1 (see Figure 6a). Computed HOMO orbitals of  $^2[CuL^2]$  exhibit  $\pi$ -character with the  $\alpha$  and  $\beta$  ones being very similar (see Figure 7a,c) and indicate that the dominating oxidation locus is on the phenolic ring and thiophenyl sulfur atom, and to a much lower extent on the copper(II) out-of-plane d-orbitals ( $d_{xz}$ ,  $d_{yz}$ ). Consequently,

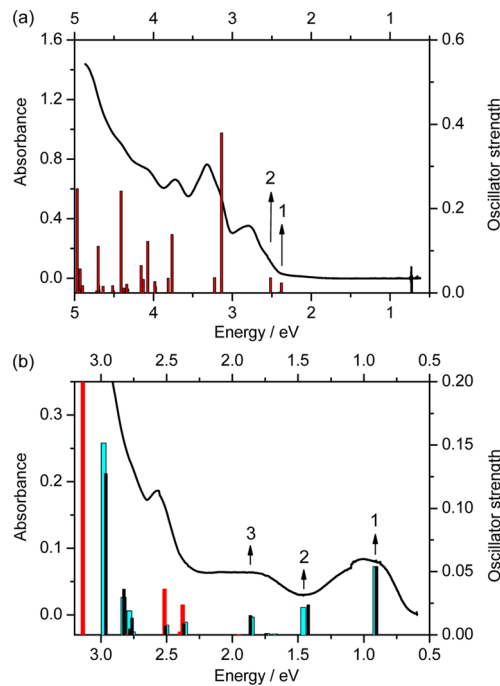


**Figure 6.** Comparison of the experimental and theoretical electronic absorption spectra: (a) Experimental and theoretical electronic transitions for  $^2[CuL^2]$  (1,  $\beta$ -HOMO–8  $\rightarrow$   $\beta$ -LUMO,  $\alpha$ -HOMO  $\rightarrow$   $\alpha$ -LUMO,  $\beta$ -HOMO  $\rightarrow$   $\beta$ -LUMO+1; 2,  $\alpha$ -HOMO  $\rightarrow$   $\alpha$ -LUMO,  $\beta$ -HOMO  $\rightarrow$   $\beta$ -LUMO+1). (b) Experimental electronic absorption spectrum for one-electron-oxidized  $[CuL^2]^+$  (black line) and electronic transitions calculated for  $^1[CuL^2]^+$  with broken symmetry treatment (black columns: 1,  $\beta$ -HOMO  $\rightarrow$   $\beta$ -LUMO; 2,  $\beta$ -HOMO–3  $\rightarrow$   $\beta$ -LUMO; 3,  $\beta$ -HOMO–5  $\rightarrow$   $\beta$ -LUMO) and  $^3[CuL^2]^+$  (cyan columns: 1,  $\beta$ -HOMO  $\rightarrow$   $\beta$ -LUMO; 2,  $\beta$ -HOMO–4  $\rightarrow$   $\beta$ -LUMO; 3,  $\beta$ -HOMO–5  $\rightarrow$   $\beta$ -LUMO); the red columns illustrate the first calculated transitions for  $^2[CuL^2]$ .

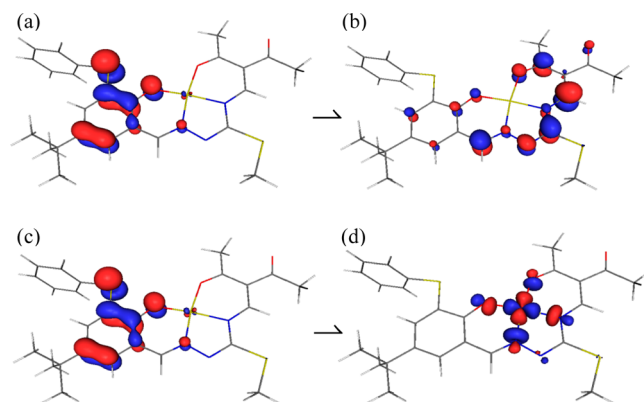


**Figure 7.** (a)  $\alpha$ -HOMO (0.4% Cu, 99.6% L<sup>2</sup>), (b)  $\alpha$ -LUMO (100% L<sup>2</sup>), (c)  $\beta$ -HOMO (0.5% Cu, 99.5% L<sup>2</sup>), and (d)  $\beta$ -LUMO+1 (39.0% Cu, 61.0% L<sup>2</sup>) for  $^2[CuL^2]$ .

the first oxidation peak can be attributed to a predominantly ligand-based oxidation.

These results, however, should be treated with care. A quite recent review by Laurent and Jacquemin<sup>39</sup> provides an assessment of performances of different functionals within the TD-DFT approach. In general, pure density functionals underestimate transition energies obtained by more sophisticated (and much more expensive) theoretical treatments (such as CAS-PT2 or CC methods), whereas hybrid functionals

including a large share of exact exchange (>50%) suffer from the opposite error. Nevertheless, B3LYP (with 20% of exact exchange) belongs to relatively successful and very frequently used functionals. We have tried to identify erroneous ghost transitions (usual artifacts of TD-DFT methods) by comparing TD-B3LYP data with other DFT functionals (such as O3LYP, BHandH, PBE1PBE, and PBEPBE functionals of Gaussian). However, these attempts afforded electron transitions in much worse agreement with experiment. We also note that our previous study<sup>1</sup> using B3LYP functional produced fairly good results for the UV-vis-NIR spectra interpretation of similar compounds.

The  $\alpha$ -LUMO (Figure 7b) and  $\beta$ -LUMO are located mainly on the ligand framework accommodating the copper atom without any metal contribution. Interestingly, the  $\beta$ -LUMO+1 (Figure 7d) orbital is of  $\sigma$  character and located on in-plane d(Cu) orbitals ( $d_{x^2-y^2}$ ) and coordinated donor atoms with antibonding d-p interactions. Consequently, the first transition in  ${}^2[\text{CuL}^2]$  can be attributed to charge transfer from the phenolic ring and thiophenyl sulfur atom to the remaining part of the tetradentate ligand and to a high extent also onto the metal d-orbitals. Other TD-DFT computed transitions at higher energies involving a large variety of MOs correlate well with experimental spectra (see Table S1 in the Supporting Information). Both triplet and singlet states were calculated for oxidized CuL<sup>2+</sup> indicating higher stability for the triplet state  ${}^3[\text{CuL}^2]^+$  by 0.1 eV (see Table S2 in the Supporting Information). The lowest energy electron transition around 0.9 eV observed for the  ${}^3[\text{CuL}^2]^+$  triplet state (see cyan column 1 in Figure 6b) is attributed to the  $\beta$ -HOMO to  $\beta$ -LUMO transition. Almost the same pattern of theoretical electronic spectrum was found for the “broken symmetry” singlet state  ${}^1[\text{CuL}^2]^+$  (see black columns in Figure 6b).

Both the  $\beta$ -HOMO of  ${}^3[\text{CuL}^2]^+$  and  $\beta$ -HOMO of  ${}^1[\text{CuL}^2]^+$  (Figure 8a,c) are similar to the  $\alpha$ -LUMO of  ${}^2[\text{CuL}^2]$  (Figure

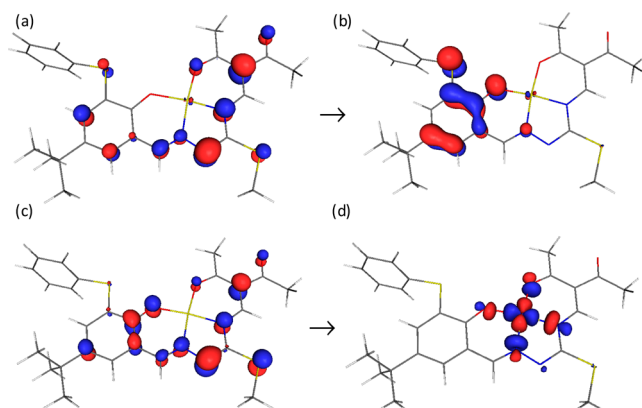


**Figure 8.** (a)  $\beta$ -HOMO of  ${}^3[\text{CuL}^2]^+$  (0.3% Cu, 99.7% L<sup>2-</sup>), (b)  $\beta$ -LUMO of  ${}^3[\text{CuL}^2]^+$  (0.4% Cu, 99.6% L<sup>2-</sup>), (c)  $\beta$ -HOMO  ${}^1[\text{CuL}^2]^+$  cation (unrestricted “broken symmetry” treatment, 0.2% Cu, 99.8% L<sup>2-</sup>), (d)  $\beta$ -LUMO  ${}^1[\text{CuL}^2]^+$  cation (unrestricted “broken symmetry” treatment, 39.9% Cu, 60.1% L<sup>2-</sup>).

7b), while  $\beta$ -LUMO of  ${}^3[\text{CuL}^2]^+$  with a triplet ground state (Figure 8b) is very similar to the  $\beta$ -HOMO for  ${}^2[\text{CuL}^2]$  (Figure 7c). Patterns of  $\beta$ -LUMO for  ${}^1[\text{CuL}^2]^+$  (unrestricted) (Figure 8d) and the  $\beta$ -LUMO+1 for  ${}^2[\text{CuL}^2]$  (Figure 7d) are also very similar.

**Catalysis.** The investigated metal complexes operate effectively (overall yields up to 85% and TONs up to 850) for the aerobic TEMPO-mediated oxidation of benzyl alcohol (BzOH) to benzaldehyde and the peroxidative oxidation (by aqueous TBHP) of benzyl alcohol to benzaldehyde (main product) and benzoic acid (Table 4, entries 1–18). The system

**Table 4. Oxidation of Primary and Secondary Alcohols Using Two Different Oxidants, TEMPO/air<sup>a</sup> and TBHP,<sup>b</sup> Catalyzed by Copper(II), Nickel(II), and Zinc(II) Complexes**

entry	catalyst	alcohol	oxidant	yield <sup>c</sup> (%)	selectivity <sup>d</sup> (%)	TON <sup>e</sup>
1	1	BzOH	TEMPO/air	6.5	>99	65
2	1	BzOH	TBHP	22.6	83	226
3	2	BzOH	TEMPO/air	70.5	>99	705
4	2	BzOH	TBHP	63.7	85	637
5	3	BzOH	TEMPO/air	3.5	>99	35
6	3	BzOH	TBHP	2.8	90	28
7	4	BzOH	TEMPO/air	5.4	>99	54
8	4	BzOH	TBHP	26.9	87	269
9	5	BzOH	TEMPO/air	85.1	>99	851
10	5	BzOH	TBHP	82.4	84	824
11	6	BzOH	TEMPO/air	80.3	>99	803
12	6	BzOH	TBHP	76.2	83	762
13	7	BzOH	TEMPO/air	72.6	>99	726
14	7	BzOH	TBHP	61.5	84	615
15	8	BzOH	TEMPO/air	3.4	>99	34
16	8	BzOH	TBHP	18.9	83	189
17	9	BzOH	TEMPO/air	73.4	>99	734
18	9	BzOH	TBHP	69.8	84	698
19	2	PhEtOH	TEMPO/air	5.9	—	59
20	5	PhEtOH	TEMPO/air	9.7	—	97

<sup>a</sup>Reaction conditions: alcohol (BzOH = benzyl alcohol; PhEtOH = 1-phenylethanol) (3.0 mmol), catalyst (3  $\mu$ mol, 0.1 mol %), TEMPO (0.15 mmol, 5 mol %), in 5.0 mL of 1:1 (v/v) MeCN/0.1 M  $\text{K}_2\text{CO}_3$  aqueous solution, 50 °C, air (1.0 atm). <sup>b</sup>Reaction conditions: alcohol (3.0 mmol), catalyst (3  $\mu$ mol, 0.1 mol %), TBHP (15 mmol), in 5.0 mL of 1:1 (v/v) MeCN/0.1 M  $\text{K}_2\text{CO}_3$  aqueous solution, 50 °C; mol % is vs substrate. <sup>c</sup>Overall yield of carbonyl products/mole of alcohol  $\times$  100%. <sup>d</sup>Selectivity (%) toward aldehyde formation is equal to the molar amount of benzaldehyde/total molar amount of products  $\times$  100%. <sup>e</sup>TON was estimated as moles of product(s)/mole of catalyst.

TEMPO/air/M (M = Ni(II), Zn(II), or Cu(II)) using complexes 1–9 exhibits a remarkably high selectivity toward the formation of benzaldehyde (>99%), while TBHP/catalyst 1–9 produces both benzaldehyde and benzoic acid, with selectivity up to 85% for aldehyde, as confirmed by mass balances.

In the oxidation of primary alcohol, the Cu<sup>II</sup> complexes (2, 5–7, and 9) exhibit high activities, whereas the Ni<sup>II</sup> complexes (1, 4, and 8) are weakly active (Table 4). The yield obtained with the Zn<sup>II</sup> complex 3 is very poor (Table 4, entries 5 and 6), since no redox reaction is expected at the Zn<sup>II</sup> site. The

combination of copper(II) complexes (**2** and **5**) and TEMPO/air was not active for the oxidation of 1-phenylethanol (PhEtOH) (secondary alcohol), and lower yields (up to 10%, Table 4, entries 19 and 20) were obtained compared to primary alcohols (up to 85%, entry 9). The low catalytic activity concerning secondary alcohols is attributed to steric hindrance and to the absence of stabilization by H-bonding of the Cu( $\text{O}-\text{C}^{\bullet}\text{RR}'$ )(TEMPOH) intermediate bearing a secondary C radical instead of a primary one,<sup>18d</sup> and is in accord with other TEMPO mediated systems.<sup>19,20</sup>

The addition of base ( $\text{K}_2\text{CO}_3$ ) has been essential for alcohol activation. Other bases such as NaOH, pyridine, or triethylamine can also be employed (Figure 9).

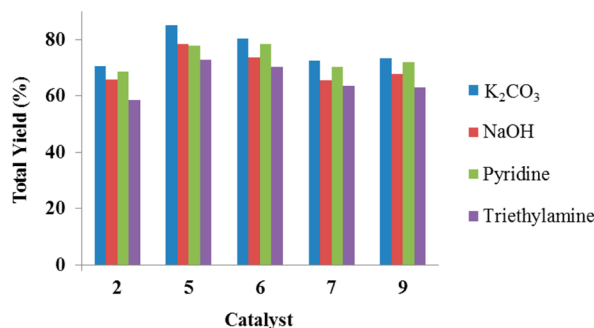


**Figure 9.** Effect of base in the aerobic oxidation of benzyl alcohol by the copper(II) complexes (**2**, **5–7**, and **9**) using TEMPO/air. Reaction conditions: benzyl alcohol (3.0 mmol), catalyst (3  $\mu\text{mol}$ , 0.1 mol %), TEMPO (0.15 mmol, 5 mol %), in 5.0 mL of 1:1 (v/v) MeCN/0.1 M base aqueous solution, 50 °C, air (1.0 atm).

However, none of the tested ones was as effective as  $\text{K}_2\text{CO}_3$ . This is consistent with the higher coordinating ability of the latter bases, compared with  $\text{K}_2\text{CO}_3$ , thus competing with the substrate and/or  $\text{O}_2$  for coordination to the catalytically active copper(II) center.

Attractive features of this catalytic system include the efficient use of air as oxidant, high yield (up to 85%) and selectivity (99%), and low loading of both TEMPO (5 mol %) and the copper(II) complexes (0.1 mol %) under mild reaction conditions (50 °C). The disadvantage of the system is that secondary alcohols (e.g., 1-phenylethanol) are barely active (10%). However, a microwave-assisted solvent-free system does allow catalytic oxidation of secondary alcohols as summarized in Table 5.

Specifically, the catalytic activities of  $\text{Cu}^{II}$ ,  $\text{Ni}^{II}$ , and  $\text{Zn}^{II}$  complexes for the oxidation of 1-phenylethanol using TBHP as oxidant at 80 °C under microwave (MW) irradiation were studied. Copper(II) complexes (**2**, **5–7**, **9**) proved to be more effective catalysts than the nickel(II) (**1**, **4**, **8**) and zinc(II) (**3**) analogues. The system also shows good substrate versatility (cyclic and aliphatic alcohols). The maximum total yields of products are achieved in the oxidation of cyclopentanol (94%), cyclohexanol (94%), cycloheptanol (87%), and cyclooctanol (81%) (Table 6, entries 1–4). These data reveal a lowering of the cyclic alcohol reactivity on increasing the number of ring carbon atoms, probably due to increased steric hindrance at the catalytic center.

In spite of being more inert toward selective oxidation, various linear aliphatic secondary alcohols can be also oxidized to the corresponding ketones (up to 43%, Table 6, entries 5–7).

**Table 5. Solvent-Free Oxidation of 1-Phenylethanol Catalyzed by Copper(II), Nickel(II), and Zinc(II) Complex TBHP/MW System<sup>a</sup>**

entry	catalyst	yield <sup>b</sup> (%)	TON <sup>c</sup>
1	<b>1</b>	23.4	234
2	<b>2</b>	63.6	636
3	<b>3</b>	2.8	28
4	<b>4</b>	28.5	285
5	<b>5</b>	95.1	951
6	<b>6</b>	92.6	926
7	<b>7</b>	83.4	834
8	<b>8</b>	19.9	199
9	<b>9</b>	67.4	674
10 <sup>d</sup>	<b>5</b>	3.7	37

<sup>a</sup>For all reactions, the oxidant was TBHP. Reaction conditions: substrate (5.0 mmol), catalyst (5  $\mu\text{mol}$ , 0.1 mol % vs substrate), TBHP (10.0 mmol, 70% in  $\text{H}_2\text{O}$ ), 80 °C, MW irradiation (10 W power), 240 min.

<sup>b</sup>Moles of product/mole of substrate  $\times$  100%. <sup>c</sup>TON was estimated as moles of product (acetophenone)/mole of catalyst.

<sup>d</sup>Diphenylamine was used as a radical trap.

The efficiency of oxidation is not affected by the position of the OH group in the aliphatic chain of substrate, as attested by the similar yields of 2-hexanone and 3-hexanone detected in the oxidations of the corresponding isomeric alcohols (Table 6, entries 6 and 7). In all cases, catalysts **5** and **6** show a higher activity over the copper(II) complex **9**.

## DISCUSSION

A number of transition metal complexes with salen type ligands ( $\text{N}_2\text{O}_2$  bis-Schiff base bis-phenolate ligands) have been shown to undergo one-electron oxidation with the formation of metal–phenoxy radical complexes. The degree of communication between the two originally equivalent phenolates is variable, and can be mediated through space, chemical bonds, or central metal ion.<sup>40–42</sup> Experimentally this communication can be estimated by electrochemical methods, as the stronger is the coupling, the stronger is the spin density delocalization in one-electron-oxidized species. We now report metal complexes  $\text{ML}^1$  and  $\text{ML}^2$  which contain ligands with one phenolate group specifically protected in positions 3 and 5 and significant  $\pi$ -delocalization in the coordinated state and describe the stability and electronic structure of their one-electron-oxidized species  $[\text{ML}^1]^+$  and  $[\text{ML}^2]^+$ .

DFT calculations of  $\text{ML}^1$  and  $\text{ML}^2$  predict that their oxidation occurs via removal of an electron from a predominantly ligand-based  $\pi^*$  orbital. Computed HOMO orbitals of  ${}^2\text{CuL}^2$  exhibit  $\pi$ -character with  $\alpha$  and  $\beta$  ones being very similar (see HOMOs in Figure 7) implying that the dominating oxidation locus is on the phenolic ring and thiophenyl sulfur atom, and to a much lesser extent on the copper(II) out-of-plane d-orbitals ( $d_{xz}$ ,  $d_{yz}$ ), so that first oxidation leads to a phenoxy radical species. The first optical transition with relevant oscillator strength corresponds mainly to that from  $\alpha$ -HOMO to  $\alpha$ -LUMO and from  $\beta$ -HOMO to  $\beta$ -LUMO+1. The  $\alpha$ -LUMO and  $\beta$ -LUMO are located mainly on the ligand framework accommodating the copper atom without any metal contribution. Interestingly the  $\beta$ -LUMO+1 orbital is of  $\sigma$  character and located on in-plane d(Cu) orbitals ( $d_{x^2-y^2}$ ) and coordinated donor atoms with antibonding d–p interactions.

Table 6. Solvent-Free Oxidation of Secondary Alcohols by the Copper(II) Complex (5, 6, 9)/TBHP/MW System<sup>a</sup>

Entry	Substrate	Product	Catalyst	Yield (%) <sup>b</sup>
1			5	94.4
			6	91.7
			9	65.2
2			5	93.7
			6	88.6
			9	60.1
3			5	86.8
			6	74.3
			9	48.9
4			5	80.6
			6	73.5
			9	37.5
5			5	43.2
			6	43.5
			9	20.6
6			5	42.6
			6	41.9
			9	19.7
7			5	40.9
			6	43.2
			9	21.8

<sup>a</sup>Reaction conditions: substrate (5.0 mmol), Cu catalyst (5  $\mu$ mol, 0.1 mol % vs substrate), TBHP (10.0 mmol, 70% in H<sub>2</sub>O), 80 °C, MW irradiation (10 W power), 240 min. <sup>b</sup>Moles of product/mole of substrate × 100%.

We have compared theoretical and experimental data for all monocharged complexes under study to find the most plausible explanation for the observed EPR and spectroelectrochemical results described above (Figures 4 and 5). The theoretical spin density distribution in  ${}^2[\text{CuL}^2]$  is mainly located on in-plane d(Cu) orbitals and adjacent coordinated N<sub>2</sub>O<sub>2</sub> atoms (Figure 10a). Similar patterns for theoretical spin density distribution in the oxidized  ${}^3[\text{CuL}^2]^+$  and  ${}^2[\text{NiL}^2]^+$  were found (Figure 10b,c). Taking into account the very similar redox behavior of both complexes in the region of the first oxidation peak (see Figure 3b) and the presence of similarly intense low-energy NIR transitions for both oxidized complexes (see Figures 4b and 5b) we can expect similar spin density distribution for  $[\text{CuL}^2]^+$  and  $[\text{NiL}^2]^+$ . This again indicates that  ${}^3[\text{CuL}^2]^+$  is a more favored structure compared to  ${}^1[\text{CuL}^2]^+$ . For  ${}^3[\text{CuL}^2]^+$  the dominant spin density is located mainly on the phenolic ring, thiophenyl sulfur, and phenolate oxygen and on the hydrazine residue nitrogen atom. Strong contribution from the Cu central atom d-orbitals and adjacent coordinated atoms is also evident (Figure 10b). The spin densities in the singlet and triplet forms of  $[\text{CuL}^2]^+$  are essentially equivalent; the only difference is that the spin densities on the Cu and phenoxy group are aligned antiparallel for the singlet state (compare also Figure S6 in the Supporting Information).

It is worth noting that different spin distributions are exhibited by the  ${}^2[\text{NiL}^1]^+$  and  ${}^2[\text{NiL}^2]^+$  structures, both experimentally and theoretically. Negligible  $\alpha$ -spin density

was found on the phenolic ring and thiomethyl sulfur in  ${}^2[\text{NiL}^1]^+$  where the  $\beta$ -spin dominates (Figure 11). The g value 2.0091 indicates a species of predominantly phenoxy radical character with contribution from the central Ni<sup>II</sup> atom with its more than half-filled (3d<sup>8</sup>) configuration (see Table S3 in the Supporting Information). DFT calculations showed that the  $\alpha$ -spin density is mainly located on Ni d-orbitals and coordinated N<sub>2</sub>O<sub>2</sub> atoms. This correlates well with the experimental EPR spectrum found at the first oxidation peak of NiL<sup>1</sup> (Figure 11a), which can be simulated with two nonequivalent nitrogens with  $a_N = 4.12$  G and  $a_N = 3.61$  G (see Figure S7 in the Supporting Information). It should be also noted that the observed spectrum can be alternatively simulated using 3H of the S-methyl group and a single meta H (based on the  $\beta$ -spin distribution). In the case of  ${}^2[\text{NiL}^2]^+$  with thiophenyl group in ortho position, a relatively narrow doublet-like EPR signal characteristic of delocalized spin was observed (Figure 11b). At low temperatures, this EPR signal becomes anisotropic with a rhombic pattern with g values characteristic of a ligand radical ( $g_1 = 2.019$ ,  $g_2 = 2.012$ ,  $g_3 = 1.999$ ) with partial delocalization of the unpaired spin onto orbitals of the nickel ion<sup>1</sup> (Figure S8 in the Supporting Information). For comparison, tetraazamacrocyclic complexes of Ni<sup>III</sup> have typically  $g_{\perp} \approx 2.00-2.05$ .<sup>43,44</sup>

The calculated spin density distribution pattern in both  ${}^2[\text{NiL}^2]^+$  and  ${}^3[\text{CuL}^2]^+$  has significant spin population on the thiophenyl sulfur atom and strong spin delocalization over a large part of the molecule, including the central atom. This

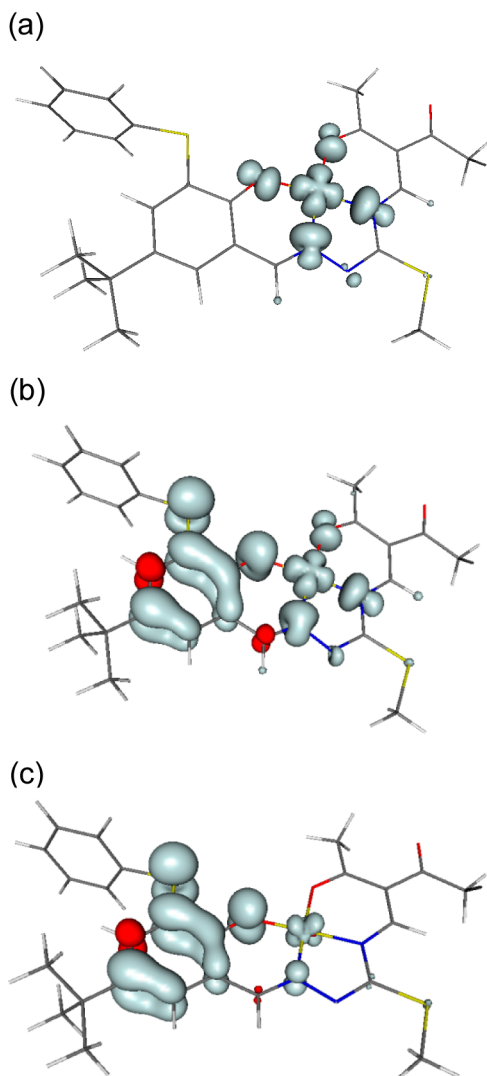


**Figure 10.** Spin density at  $\pm 0.003$  au level for (a)  $^2[\text{CuL}^2]$ , (b)  $^3[\text{CuL}^2]^+$  cation triplet, and (c)  $^2[\text{NiL}^2]^+$  cation doublet ( $\alpha$ -spin density in gray,  $\beta$ -spin density in red).

distribution is presumably responsible for the increased stability of one-electron oxidized complexes  $[\text{ML}^2]^+$  and their reversible anodic oxidation even at very low scan rates. The experimental room temperature spectroelectrochemical data can be reliably interpreted if  $^3[\text{CuL}^2]^+$  and  $^2[\text{NiL}^2]^+$  oxidation states (computed for gas phase) are taken into account. Although copper(II)-phenoxy radical species are known to exhibit antiferromagnetic exchange interactions between  $\text{Cu}^{II}$  and the phenoxy radical, they can be EPR active, showing the  $S = 1$  ground state with a weak ferromagnetic interaction between  $\text{Cu}^{II}$  and phenoxy radical as already reported for a series of copper(II)-phenoxy radical complexes with tripodal ligands.<sup>10</sup> If this were the case for our  $^3[\text{CuL}^2]^+$  in solution, then such a spin triplet could in principle be observed by EPR. The inability to see EPR in our experiment might be due to the properties of the triplet being unsuitable for observation by conventional EPR (e.g., its zero-field splitting ( $D$  value) might be larger than the X-band microwave energy,  $\sim 0.3 \text{ cm}^{-1}$ ) and by the temperature limit (100 K) in our laboratory.

The formal oxidation number of  $\text{M} = \text{Ni}$  and  $\text{Cu}$  atoms in  $[\text{ML}^{1-2}]$ , is +II and in  $[\text{ML}^{1-2}]^+$  it is +III. Nevertheless, in the case of “noninnocent” ligands<sup>45</sup> the situation is much more

complicated and the real physical (or spectroscopic) oxidation number differs from the formal one.<sup>46,47</sup> The physical oxidation state in transition metal complexes may be ascribed according to the number of their d-electrons (more exactly d-electron populations).  $\text{Ni}^{2+}$  and  $\text{Cu}^{2+}$  ions have eight and nine d-electrons, respectively, and d-orbitals’ populations in nickel(II) and copper(II) complexes with “innocent” ligands are approaching these values accordingly. Based on Mulliken population analysis (MPA), this value varies with spin multiplicity between 8.16 and 8.34 both for  $\text{NiL}^1$  and  $\text{NiL}^2$  neutral complexes and for their one-electron-oxidized species (see Table S3 in the Supporting Information), which points to the physical oxidation number +II for all these systems. Energy data of DFT optimized geometries indicate the higher stability of  $\text{NiL}^1$  complex in the singlet spin state, whereas  $\text{NiL}^2$  complex is more stable in the triplet spin state (see Table S2 in the Supporting Information). According to experimental data,  $\text{NiL}^1$  possesses a singlet ground state both in the solid state and in solution as well, since the compound displays a “normal”  $^1\text{H}$  NMR spectrum without detectable paramagnetic shifts or line broadening of the proton resonances even at room temperature (such effects are generally seen for NMR of authentic paramagnetic Ni(II) complexes).<sup>48</sup> MPA of  $\text{CuL}^1$  and  $\text{CuL}^2$  neutral complexes and their one-electron-oxidized species gives d-electron populations at Cu of ca. 9.2 (see Table S3 in the Supporting Information), which implies their physical Cu oxidation number of +II as well (independent of their charge and spin state).

Both  $[\text{CuL}^1]^+$  and  $[\text{CuL}^2]^+$  in the triplet spin state are more stable than their singlet state counterparts (including the “broken symmetry” structure obtained within unrestricted Kohn–Sham formalism, see Table S2 in the Supporting Information). The “noninnocent” character of our ligands is very well illustrated by only small variations in M atomic charges during one-electron oxidation indicating the electron removal prevailingly from the ligands (Table S3 in the Supporting Information). According to MPA,  $^2[\text{NiL}^1]^+$  has 1.62 unpaired  $\alpha$ -electrons (positive spin) at the Ni atom, which corresponds nearly to the triplet state with two unpaired electrons. As the doublet ground state of the whole complex cation indicates a single unpaired electron with  $\alpha$ -spin ( $S_{\text{total}} = 1/2$ ), an antiferromagnetic coupling of the  $\alpha$ -spin of the  $\text{Ni}^{II}$  ( $S_{\text{Ni}} = 1$ ) and the radical  $\beta$ -spin of the ligand ( $S_{\text{ligand}} = -1/2$ ) may be expected. Thus the ligand must have 0.62 unpaired  $\beta$ -electron (negative spin). The formation of a  $^2[\text{NiL}^1]^+$  complex cation might be explained under the assumption of a neutral  $[\text{NiL}^1]$  complex in the triplet spin state and its oxidation corresponding to an  $\alpha$ -electron removal from the ligand. Therefore, the  $\beta$ -electron density prevails on the ligand in  $[\text{NiL}^1]^+$  due to vanishing  $\alpha$ -electron density transfer from d-orbitals of nickel. Finally, the  $[\text{NiL}^1]^+$  complex cation can be therefore understood as a system with  $\alpha$ -spin density (1.62 e) concentrated at Ni(II) central atom and about three times lower  $\beta$ -spin density concentrated at the ligand (the positive and negative spins are separated in space; they do not occupy the same orbital, but interact with each other in an antiferromagnetic manner; see also Figure 11a). This picture is supported by the antibonding character of Ni–ligand frontier molecular orbitals as well.

As MPA gives only small unpaired  $\alpha$ -electron density at Ni atom of  $^2[\text{NiL}^2]^+$  and (ground state)  $^3[\text{NiL}^2]$  species, the  $\alpha$ -spin density is localized prevailingly on the ligand (1.90 unpaired  $\alpha$ -electrons in neutral triplet complex and 0.95

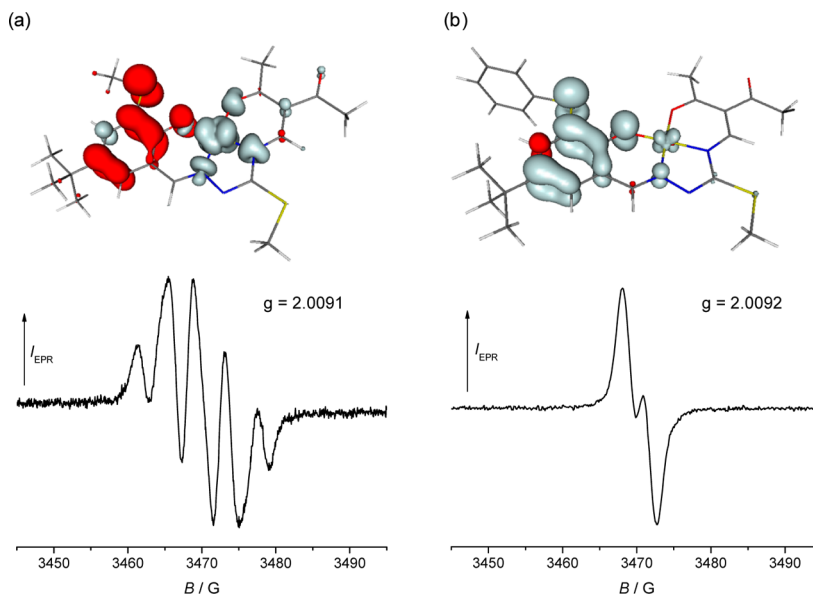


**Figure 11.** Spin density at  $\pm 0.003$  au level for (a)  ${}^2[\text{NiL}^1]^+$  and (b)  ${}^2[\text{NiL}^2]^+$  ( $\alpha$ -spin density in gray,  $\beta$ -spin density in red) with their corresponding EPR spectra measured at the first anodic peak (modulation amplitude 0.5 G).

unpaired  $\alpha$ -electron after one  $\alpha$ -electron removal during oxidation).

According to MPA, both  ${}^3[\text{CuL}^1]^+$  and  ${}^3[\text{CuL}^2]^+$  have 0.64 unpaired  $\alpha$ -electron (positive spin) at Cu atoms. As the ground triplet spin state of the whole complex cation corresponds to two  $\alpha$ -electrons, ca. twice higher  $\alpha$ -electron density (1.36 e) remains on the ligands. As the Cu spin density in both neutral complexes is the same as in the corresponding complex cations, this implies 0.36 unpaired  $\alpha$ -electron on ligands. Consequently, one  $\beta$ -electron must be removed from the ligand during oxidation. This is in agreement with higher  $\beta$ -HOMO energies ( $-0.1863$  au in  ${}^2[\text{CuL}^1]$  and  $-0.1873$  au in  ${}^2[\text{CuL}^2]$ ) in comparison with the  $\alpha$ -HOMO ones ( $-0.1871$  au and  $-0.1882$  au, respectively) enabling preferred  $\beta$ -electron removal.

The TEMPO-mediated aerobic oxidation catalyzed by copper S-methylisothiocarbazole complexes involves a similar pathway to that previously proposed<sup>18</sup> for other Cu/air/TEMPO systems of the galactose oxidase type. Concerning the  $M^{II}L^{1-2}$  complexes, the best catalyst for the oxidation of benzyl alcohol is  $\text{CuL}^2$  (**5**), in both TBHP and air/TEMPO systems. The replacement of the *tert*-Bu group in  $\text{CuL}$  complex (**9**) in the ortho position of the phenolic moiety by a thioaryl group ( $-SPh$ ) in  $\text{CuL}^2$  (**5**) or without any substituent group (**6**) can produce better catalysts mimicking the active metal sites of copper oxidases. The higher catalytic yield is attributed to the radical stabilizing effect by electron spin-delocalization into the thiophenyl group. The presence of the  $-SCH_3$  group in the other tetradentate  $N_2O_2$  ligands (**2**, **7**, **9**) decreases the reactivity of the corresponding complexes in the alcohol oxidation compared to an unsubstituted derivative (**6**). This decrease may be due to the lack of electron delocalization into the  $-SCH_3$  group in these complexes, and/or the  $-SCH_3$  group may occupy the axial coordination site of the copper atom of the neighboring molecule and influence in such a way the reactivity of the metal center.

As mentioned above, the system based on copper S-methylisothiocarbazole complexes and air/TEMPO is not active for the oxidation of secondary alcohols. However, by applying the recently developed<sup>20</sup> microwave-assisted

oxidation of secondary alcohols in a solvent-free system using TBHP as oxidant, we have shown that secondary alcohols are better oxidized to ketones with TBHP as oxidant under microwave irradiation. An increase of the catalyst amount greatly enhances the product yield from 51 to 95% for the respective amounts of 1 and 5  $\mu\text{mol}$  of catalyst **5**, but with a decrease of the TON from 2540 to 951 (Figure S9 in the Supporting Information).

Another important factor in system performance concerns the relative amounts of oxidant (TBHP). Increasing the  $n(\text{TBHP})/n(\text{catalyst})$  molar ratio from 1000 to 2000 (which corresponds respectively to 5 and 10 mmol of TBHP) leads to a yield enhancement from 66% to 95%, for catalyst **5** (Figure 12). However, further increase of the oxidant amount (above

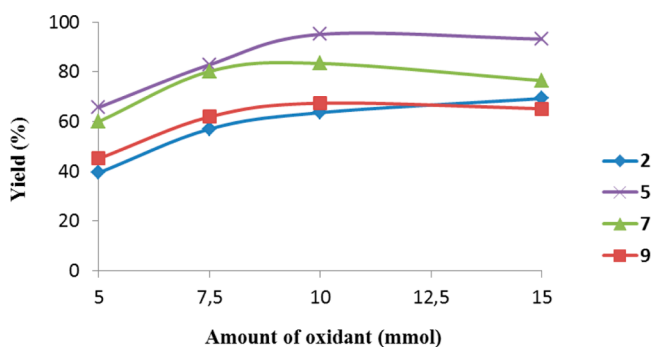


**Figure 12.** Effect of the amount of oxidant (TBHP) on the total yield in the peroxidative oxidation of 1-phenylethanol to acetophenone by copper complexes.

10 mmol) does not result in a higher activity in the case of complexes **5** and **9**, and even lowers the performance of catalyst **7** (Figure 12).

In order to determine the mechanism of the peroxidative oxidation of secondary alcohols under microwave irradiation, we have tested the influence of a radical trap (diphenylamine)<sup>49</sup> on the oxidation of 1-phenylethanol by the **5**/TBHP/MW system. The addition of diphenylamine in equimolar amounts

relative to the substrate results in a pronounced decrease of the yield from 95% to 4% (Table 5, entries 5 vs 10). This observation provides strong evidence for the involvement of a free radical mechanism in the oxidation of secondary alcohols, which eventually proceeds with the participation of *t*-BuO<sup>•</sup> and *t*-BuO<sup>•</sup> radicals.<sup>50</sup>

The detailed mechanism of TEMPO-catalyzed oxidation of alcohols ( $\text{RCH}_2\text{OH}$ ) with our copper(II) S-methylisothiosemicarbazones could not be established. The reaction could proceed via the mechanism proposed by Semmelhack (alcohol being oxidized by uncoordinated TEMPO<sup>+</sup> formed upon oxidation of TEMPO by Cu<sup>II</sup>)<sup>51</sup> or by that of Sheldon (copper-centered oxidative dehydrogenation by TEMPO of the alkoxide ligand  $\text{RCH}_2\text{O}^-$  derived from the alcohol, to form a  $\text{RC}^{\bullet}\text{HO}$  radical and TEMPOH)<sup>19</sup> or related ones discussed on the basis of theoretical studies.<sup>18*h,i,52*</sup> Electron transfer from the  $\text{RC}^{\bullet}\text{HO}$  radical to Cu<sup>II</sup> leads to the aldehyde RCHO and Cu<sup>I</sup>. TEMPO mediated oxidation of Cu<sup>I</sup> regenerates Cu<sup>II</sup>, whereas TEMPO is regenerated upon aerobic oxidation of TEMPOH.<sup>18–20,51–53</sup> Furthermore, the antioxidant ability of TEMPO to suppress the overoxidation of aldehyde to acid is also known, acting as a radical scavenger and terminating free radical chains.<sup>53</sup>

The coordination of the alkoxide  $\text{RCH}_2\text{O}^-$  derived from the benzyl alcohol to the copper catalyst precursor is suggested in our systems by the detection of possible carbonate adducts assigned as  $[\text{CuL}^5 + \text{RCH}_2\text{O}^- + \text{KHCO}_3 + \text{H}^+]^+$  ( $m/z = 753$ , 10%) and  $[\text{CuL}^5 + \text{RCH}_2\text{O}^- + \text{NaHCO}_3 + \text{H}^+]^+$  ( $m/z = 738$ , 5%) in the ESI-MS(+) spectra of reaction solutions (diluted with MeOH) containing CuL<sup>5</sup>, benzyl alcohol, and TEMPO in MeCN/aqueous solution of K<sub>2</sub>CO<sub>3</sub>. The formation of the simple carbonate adduct  $[\text{CuL}^5 + \text{KHCO}_3 + \text{H}^+]^+$  ( $m/z = 646$ , 10%) also appears to be detected in our system and in other TEMPO/copper catalysts which can present the simultaneous coordination of ligands, TEMPO, and/or benzyl alkoxide to Cu(II).<sup>18a</sup>

The above-discussed mechanisms are distinct from that of galactose oxidase, which catalyzes the oxidation of D-galactose to D-galacto-hexodialdose wherein a protein-bound phenoxy radical, coordinated to mononuclear copper, behaves as a H-atom abstractor from the alkoxide ligand.<sup>18*b,19*</sup> In our copper system, such a role is believed to be played by TEMPO and not by the S-methylisothiosemicarbazone ligand.

## CONCLUSION

Template condensation of 5-*tert*-butyl-2-hydroxy-3-methylsulfanylbenzaldehyde S-methylisothiosemicarbazone with pentane-2,4-dione and triethyl orthoformate resulted in metal complexes of the type M<sup>II</sup>L<sup>1</sup>, where M = Ni, Cu and H<sub>2</sub>L<sup>1</sup> = 9-(2'-hydroxy-3'-methylthio-5'-*tert*-butylphenyl)-6-methylthio-3-acetyl-5,7,8-triazanona-3,6,8-trien-2-one. Demetalation of Ni<sup>III</sup>L<sup>1</sup> with gaseous hydrogen chloride in chloroform afforded the metal-free ligand H<sub>2</sub>L<sup>1</sup>, which was then used for the synthesis of [Zn<sup>II</sup>L<sup>1</sup>]<sub>2</sub>. In a similar way starting from 5-*tert*-butyl-2-hydroxy-3-phenylsulfanylbenzaldehyde, S-methylisothiosemicarbazone metal complexes ML<sup>2</sup>, where M = Ni, Cu and H<sub>2</sub>L<sup>2</sup> = 9-(2'-hydroxy-3'-phenylthio-5'-*tert*-butylphenyl)-6-methylthio-3-acetyl-5,7,8-triazanona-3,6,8-trien-2-one, have been synthesized. The five metal complexes and the prepared ligand were characterized by spectroscopic methods (IR, UV-vis, and NMR spectroscopy), X-ray crystallography, and DFT calculations.

A marked stabilization of phenoxy radical was observed in one-electron-oxidized complexes  $[\text{ML}^2]^+$  at room temperature, as demonstrated by cyclic voltammetry, EPR spectroscopy, and UV-vis-NIR spectroelectrochemical measurements. The optical spectrum of  $[\text{CuL}^2]^+$  showed two maxima at 678 and 1217 nm comparable to those for native enzymes. In contrast to CuL<sup>1</sup> with quasireversible redox behavior, upon oxidation of CuL<sup>2</sup>, where (L<sup>2</sup>)<sup>2-</sup> is a tetradentate ligand with –SPh group in ortho position to phenolic oxygen, a fully reversible redox couple was observed for the first electron transfer wave. The lifetime of the oxidized CuL<sup>2</sup> was determined to be about 300 s, confirming a stabilization effect of the –SPh group. The calculated spin density distribution pattern in  ${}^3[\text{CuL}^2]^+$  and  ${}^2[\text{NiL}^2]^+$  shows a significant amount of spin population on the thiophenyl sulfur atom and strong spin delocalization over a large part of the molecule including the central atom. This delocalization is presumably responsible for the increased stability of one-electron-oxidized complexes  $[\text{ML}^2]^+$ . Similar patterns for theoretical spin density distribution in the oxidized  ${}^3[\text{CuL}^2]^+$  and  ${}^2[\text{NiL}^2]^+$  were found. The spin density is located mainly on the phenolic ring, thiophenyl sulfur, and phenolate oxygen and on the hydrazine residue nitrogen atom. It should be stressed that for CuL<sup>2</sup> we observed reversible redox behavior both for oxidation and for reduction indicating the existence of three stable redox states in analogy to galactose oxidase, namely, Cu<sup>I</sup>-ligand, Cu<sup>II</sup>-ligand, and Cu<sup>II</sup>-ligand radical forms.<sup>54</sup>

The study also showed that the copper(II) complexes are more active catalysts than the nickel(II) and zinc(II) analogues for the oxidation of primary and secondary alcohols. Benzyl alcohol was effectively oxidized to benzaldehyde in the cases of O<sub>2</sub>/TEMPO and TBHP systems, whereas secondary alcohols were better oxidized to ketones with TBHP as oxidant under microwave irradiation. The highest efficiency of CuL<sup>2</sup> (5) in the air/TEMPO system is attributed to the radical stabilizing effect by electron spin-delocalization into the thiophenyl group. The complex serves as a good functional model of the galactose oxidase. Apart from the high efficiency in terms of yields and selectivity, important features of the present aerobic and peroxidative oxidations of alcohols include solvent-free operation or the use of aqueous reaction medium, as well as environmentally friendly oxidants at mild reaction temperatures (50–80 °C).

## EXPERIMENTAL SECTION

**Starting Materials.** 5-*tert*-Butyl-2-hydroxy-3-methylsulfanylbenzaldehyde and 5-*tert*-butyl-2-hydroxy-3-phenylsulfanylbenzaldehyde were prepared by following the literature protocols.<sup>55</sup> Pentane-2,4-dione and triethyl orthoformate were purchased from Fluka and distilled before use. Cu(acac)<sub>2</sub> was purchased from Aldrich and used as received. S-Methylisothiosemicarbazide hydroiodide was synthesized by following the literature procedure.<sup>56</sup> 5-*tert*-Butyl-2-hydroxy-3-methylsulfanylbenzaldehyde S-methylisothiosemicarbazone and 5-*tert*-butyl-2-hydroxy-3-phenylsulfanylbenzaldehyde S-methylisothiosemicarbazone were prepared by condensation reaction of equimolar amounts of 5-*tert*-butyl-2-hydroxy-3-methyl(or phenyl)-sulfanylbenzaldehyde and S-methylisothiosemicarbazide hydroiodide in EtOH/H<sub>2</sub>O 1:1 followed by addition of equivalent amount of Na<sub>2</sub>CO<sub>3</sub>. Ni(acac)<sub>2</sub>·2H<sub>2</sub>O was prepared by following the procedure reported for Zn(acac)<sub>2</sub>·H<sub>2</sub>O<sup>57</sup> and dehydrated by heating in vacuo at 90 °C for 12 h. Dichloromethane (p.a.), tetra-*n*-butylammonium hexafluorophosphate (TBAPF<sub>6</sub>), (p.), both purchased from Fluka, and ferrocene (98.0%) purchased from Merck were used as received.

Table 7. Crystal Data and Details of Data Collection for  $\text{NiL}^1\cdot0.5\text{Hacac}$ ,  $\text{CuL}^1\cdot0.5\text{Hacac}$ ,  $[\text{ZnL}^1]_2$ ,  $\text{H}_2\text{L}^1$ , and  $\text{NiL}^2$ 

	$\text{NiL}^1\cdot0.5\text{Hacac}$	$\text{CuL}^1\cdot0.5\text{Hacac}$	$[\text{ZnL}^1]_2$	$\text{H}_2\text{L}^1$	$\text{NiL}^2$
empirical formula	$\text{C}_{22.5}\text{H}_{29}\text{NiN}_3\text{O}_4\text{S}_2$	$\text{C}_{22.5}\text{H}_{29}\text{CuN}_3\text{O}_4\text{S}_2$	$\text{C}_{40}\text{H}_{50}\text{Zn}_2\text{N}_6\text{O}_6\text{S}_4$	$\text{C}_{20}\text{H}_{27}\text{N}_3\text{O}_3\text{S}_2$	$\text{C}_{25}\text{H}_{27}\text{NiN}_3\text{O}_3\text{S}_2$
FW	528.32	533.15	969.84	421.57	540.33
space group	$Pccn$	$C2/c$	$P2_1/n$	$C2/c$	$P2_1/c$
$a$ [Å]	7.6021(5)	26.6516(18)	9.4262(16)	17.0432(17)	19.402(3)
$b$ [Å]	33.502(2)	6.8783(4)	13.876(3)	7.7185(7)	17.236(2)
$c$ [Å]	20.6974(12)	26.8644(19)	15.947(4)	32.514(3)	7.4354(9)
$\beta$ [deg]		98.230(3)	92.035(7)	99.084(8)	96.593(9)
$V$ [Å <sup>3</sup> ]	5271.3(6)	4874.0(6)	2084.6(8)	4223.5(7)	2470.1(5)
$Z$	8	8	2	8	4
$\lambda$ [Å]	0.71073	0.71073	0.71073	0.71073	0.71073
$\rho_{\text{calcd}}$ [g cm <sup>-3</sup> ]	1.331	1.453	1.545	1.326	1.453
crystal size, mm [mm <sup>3</sup> ]	0.10 × 0.10 × 0.05	0.18 × 0.15 × 0.03	0.15 × 0.11 × 0.10	0.20 × 0.13 × 0.08	0.30 × 0.30 × 0.01
$T$ [K]	200(2)	100(2)	100(2)	100(2)	100(2)
$\mu$ [mm <sup>-1</sup> ]	0.926	1.101	1.406	0.278	0.987
R1 <sup>a</sup>	0.0812	0.0364	0.0665	0.0513	0.0651
wR2 <sup>b</sup>	0.2314	0.0948	0.1514	0.1322	0.1688
GOF <sup>c</sup>	1.063	1.053	1.082	1.026	1.048

<sup>a</sup>R1 =  $\sum ||F_o| - |F_c|| / \sum |F_o|$ . <sup>b</sup>wR2 = { $\{\sum [w(F_o^2 - F_c^2)] / \sum [w(F_o^2)^2]\}^{1/2}$ }. <sup>c</sup>GOF = { $\{\sum [w(F_o^2 - F_c^2)] / (n - p)\}^{1/2}$ }, where  $n$  is the number of reflections and  $p$  is the total number of parameters refined.

**Analytical and Spectroscopic Measurements.** <sup>1</sup>H NMR spectra were recorded at 298 K on a Bruker FT NMR spectrometer Avance III 500 MHz at operating frequency 500.32 MHz. The C, H, N elemental analyses were performed by the Laboratory for Elemental Analysis, Faculty of Chemistry, University of Vienna, by using a Perkin-Elmer 2400 CHN elemental analyzer. IR spectra were measured on a Bruker Vertex 70 FT-IR-spectrometer by means of attenuated total reflection (ATR) technique. Electrospray ionization mass spectrometry (ESI-MS) measurements were carried out with a Bruker Esquire 3000 instrument; the samples were dissolved in methanol.

All cyclovoltammetric experiments were performed at room temperature under nitrogen atmosphere. A standard three electrode arrangement of a platinum wire as working electrode, a platinum wire as counter electrode, and silver wire pseudoreference electrode was used. Sample solutions with approximate concentration of 0.5 mM were prepared with 0.2 M TBAPF<sub>6</sub> supporting electrolyte in CH<sub>2</sub>Cl<sub>2</sub> or acetonitrile. The cyclovoltammetric measurements were carried out with a PAR potentiostat-galvanostat model 273A in a glovebox (water and oxygen less than 1 ppm). Decamethylferrocene (DmFc) was used as an internal standard. Spectroelectrochemical experiments of the investigated compounds with simultaneous UV-vis and ESR measurements were carried out in a Varian flat spectroelectrochemical cell using platinum mesh as a working electrode. Platinum wire served as a counter electrode and a silver wire calibrated against DmFc<sup>+</sup>/DmFc redox couple as a pseudoreference electrode. The cell was filled in a glovebox and tightly closed, and in situ spectroelectrochemical experiments were performed in the optical EPR cavity (ER4104OR, Bruker, Germany). The EPR spectra were recorded on an X-band EMX ESR spectrometer (Bruker, Germany). For in situ ESR/UV-vis-NIR spectroelectrochemical studies, diode-array UV-vis/NIR spectrometer system TIDAS (J&M, Aalen Germany) or Avantes UV-vis/NIR spectrometer and potentiostat Heka PG 284 (HEKA Elektronik, Germany) were used. Spectrometers were triggered using the electrochemical software package PotMaster v2. As source of light, halogen and deuterium lamps were used (AvaLight-DH-S-BAL).

**Crystallographic Structure Determination.** X-ray diffraction measurements were performed with Bruker X8 APEX II CCD diffractometer. Single crystals were positioned at 50, 35, 35, 40, and 40 mm from the detector, and 999, 965, 791, 1230, and 1337 frames were measured, each for 60, 10, 20, 60, and 60 s over 1° scan width for  $\text{NiL}^1\cdot0.5\text{Hacac}$ ,  $\text{CuL}^1\cdot0.5\text{Hacac}$ ,  $[\text{ZnL}^1]_2$ ,  $\text{H}_2\text{L}^1$ , and  $\text{NiL}^2$ , respectively. The data were processed using SAINT software package.<sup>58</sup> Crystal data, data collection parameters, and structure refinement details are given in Table 7. The structures were solved by direct methods and

refined by full-matrix least-squares techniques. Non-hydrogen atoms were refined with anisotropic displacement parameters except those of disordered cocrystallized pentane-2,4-dione molecule. H atoms were placed at calculated positions and refined as riding atoms in the subsequent least-squares model refinements. The isotropic thermal parameters were estimated to be 1.2 times the values of the equivalent isotropic thermal parameters of the non-hydrogen atoms to which hydrogen atoms were bonded. SHELXS-97 was used for structure solution and SHELXL-97 for refinement;<sup>59</sup> molecular diagrams were produced with ORTEP.<sup>60</sup> Refinement of the structures revealed that  $-\text{C}(\text{CH}_3)_3$  group in  $\text{NiL}$  occupies two statistically disordered positions with 50% probability. The same approach, in combination with the available tools (PART, DFIX, and SADI) of SHELXL97, was used for resolving the disorder in cocrystallized pentane-2,4-dione present in the structures of both  $\text{NiL}^1\cdot0.5\text{Hacac}$  and  $\text{CuL}^1\cdot0.5\text{Hacac}$ . The fractional contributions of the two positions are in 0.4:0.6 and 0.5:0.5 ratio, for  $\text{NiL}^1$  and  $\text{CuL}^1$ , respectively. Crystallographic data for the structural analysis has been deposited with the Cambridge Crystallographic Data Centre, CCDC No. 915401–915405 for compounds  $\text{NiL}^1\cdot0.5\text{Hacac}$  (Hacac = pentane-2,4-dione),  $\text{H}_2\text{L}^1$ ,  $\text{CuL}^1\cdot0.5\text{Hacac}$ ,  $\text{ZnL}^1$ , and  $\text{NiL}^2$ , respectively.

**DFT Calculations.** The geometries of the transition metal complexes  $M^{II}\text{L}^1$  and  $M^{II}\text{L}^2$  ( $M = \text{Ni, Cu}$ ) as well as of their one-electron-oxidized species in the singlet, doublet, and/or triplet spin states were optimized at the B3LYP level of theory (starting from experimental X-ray structures) without any symmetry restrictions using the Gaussian03 program package.<sup>61</sup> The singlet states have been treated using both restricted and unrestricted formalism. The standard 6-311G\* basis set was used for transition metal, sulfur, oxygen, and nitrogen atoms and 6-31G\* for the remaining atoms. The stability of the obtained structures has been tested by vibrational analysis (no imaginary vibrations). Relative energies of various charge and spin states of the same complex have been corrected using restricted open-shell single-point calculations<sup>62</sup> except of “broken symmetry” singlet state where the energy difference between singlet ( $E_S$ ) and triplet ( $E_T$ ) states is evaluated as

$$E_S - E_T = (E_{BS} - E_{uT}) / (1 - 0.5\langle S^2 \rangle_{BS}) \quad (1)$$

where  $E_{uT}$  is an open-shell energy of triplet state and  $E_{BS}$  and  $\langle S^2 \rangle_{BS}$  are energy and spin-square values of the “broken symmetry” singlet state, respectively (see Table S4 in the Supporting Information).<sup>62,63</sup>

Based on the optimized B3LYP geometries, the vertical transition energies and oscillator strengths between the initial and final electron states for electronic absorption spectra were computed by the TD-

DFT method. All the basis sets used are included in the Gaussian03 library.<sup>61</sup> For d-orbital descriptions, the *xy* plane is defined by O1, O2, N1, and N3 atoms coordinating the central transition metal atom (Cu or Ni).

**Synthesis of Metal Complexes and Ligand: Ni<sup>II</sup>L<sup>1</sup>.** A suspension of 5-*tert*-butyl-2-hydroxy-3-methylsulfanylbenzaldehyde S-methylisothiosemicarbazone (0.96 g, 3.1 mmol) and Ni(acac)<sub>2</sub> (0.75 g, 2.9 mmol) in pentane-2,4-dione (20 mL) and triethyl orthoformate (5 mL) were heated under argon atmosphere at 107 °C for 8 h. The reaction mixture was allowed to cool to room temperature. The red precipitate formed was filtered off, redissolved in methylene chloride, and filtered. The filtrate was evaporated under reduced pressure to ca. 15 mL, and then the product was precipitated by excess ethanol, filtered off, and dried in vacuo. Yield: 0.64 g, 45.3%. Calcd for C<sub>20</sub>H<sub>22</sub>NiN<sub>3</sub>O<sub>3</sub>S<sub>2</sub>·0.5H<sub>2</sub>O ( $M_r$  487.26 g/mol), %: C, 49.30; H, 5.38; N, 8.62; S, 13.16. Found, %: C, 49.24; H, 5.02; N, 8.86; S, 13.46. <sup>1</sup>H NMR (500.32 MHz, CDCl<sub>3</sub>): δ = 8.12 (s, 1H, CH=N), 7.92 (s, 1H, =CH-N), 7.31 (s, 1H, Ar), 7.08 (s, 1H, Ar), 2.72 (s, 3H, CH<sub>3</sub>), 2.68 (s, 3H, CH<sub>3</sub>), 2.49 (s, 3H, SCH<sub>3</sub>), 2.43 (s, 3H, SCH<sub>3</sub>), 1.36 (s, 9H, C(CH<sub>3</sub>)<sub>3</sub>). IR spectrum (ATR, selected bands,  $\nu_{\text{max}}$ ): 2865, 1655, 1582, 1522, 1297, 1171, 942, 622 cm<sup>-1</sup>. UV-vis in CHCl<sub>3</sub>, λ, nm ( $\epsilon$ , M<sup>-1</sup> cm<sup>-1</sup>): 474 (5169), 379 (17700), 269 (47300). X-ray diffraction quality single crystals of Ni<sup>II</sup>L·0.5Hacac were grown from solution of Ni<sup>II</sup>L in pentane-2,4-dione.

**Cu<sup>II</sup>L<sup>1</sup>.** A suspension of 5-*tert*-butyl-2-hydroxy-3-methylsulfanylbenzaldehyde S-methylisothiosemicarbazone (0.75 g, 2.4 mmol) and Cu(acac)<sub>2</sub> (0.57 g, 2.2 mmol) in pentane-2,4-dione (20 mL) and triethyl orthoformate (5 mL) were heated under argon atmosphere at 107 °C for 8 h. The reaction mixture was allowed to cool slowly to room temperature. The brown crystals were filtered off, redissolved in methylene chloride, and filtered. The filtrate was evaporated under reduced pressure to ca. 15 mL, and then the product was precipitated by excess ethanol, filtered off, and dried in vacuo. Yield: 0.40 g, 44.0%. Calcd for C<sub>20</sub>H<sub>25</sub>CuN<sub>3</sub>O<sub>3</sub>S<sub>2</sub> ( $M_r$  483.11 g/mol), %: C, 49.72; H, 5.22; N, 8.70; S, 13.27. Found, %: C, 49.60; H, 5.21; N, 8.54; S, 12.89. ESI-MS (CH<sub>3</sub>OH) positive: m/z 483 [M + H]<sup>+</sup>, 505 [M + Na]<sup>+</sup>, 521 [M + K]<sup>+</sup>. IR spectrum, (ATR, selected bands,  $\nu_{\text{max}}$ ): 2961, 1660, 1586, 1510, 1464, 1429, 1364, 1290, 1165, 1120, 933, 781, 645 cm<sup>-1</sup>. UV-vis in CHCl<sub>3</sub>, λ, nm ( $\epsilon$ , M<sup>-1</sup> cm<sup>-1</sup>): 447 (5567), 375 (16406), 375 (16406), 332 (17126), 295 (37504). The crystals grown in pentane-2,4-dione were of X-ray diffraction quality.

**H<sub>2</sub>L<sup>1</sup>.** Hydrogen chloride was bubbled through a solution of NiL<sup>1</sup> (0.10 g, 0.20 mmol) in chloroform (50 mL). The red color of the solution faded gradually and became yellow. Water (200 mL) was added, and after vigorous stirring the organic layer was separated from the aqueous phase using a separating funnel. This operation was repeated 5–6 times to ensure the removal of nickel(II) from the organic layer. The chloroform was evaporated under reduced pressure almost to dryness, and to the remaining residue was added ethanol (10–15 mL). The solution was allowed to stand at 4 °C overnight. The crystals formed were separated by filtration and washed with cold ethanol (5 mL). The crystallized product was also suitable for X-ray diffraction measurement. Yield: 0.08 g, 95.0%. Mp: 190 °C. Calcd for C<sub>20</sub>H<sub>22</sub>N<sub>3</sub>O<sub>3</sub>S<sub>2</sub>·0.4H<sub>2</sub>O ( $M_r$  428.35 g/mol), %: C, 56.03; H, 6.54; N, 9.81; S, 14.93. Found, %: C, 56.22; H, 6.37; N, 9.60; S, 14.79. ESI-MS (CH<sub>3</sub>OH) positive: m/z 422 [M + H]<sup>+</sup>, 444 [M + Na]<sup>+</sup>, 460 [M + K]<sup>+</sup>. IR spectrum, (ATR, selected bands,  $\nu_{\text{max}}$ ): 3001, 2953, 2919, 2865, 1632, 1571, 1534, 1425, 1374, 1279, 1185, 1137, 958, 743, 669, 613 cm<sup>-1</sup>. UV-vis in DMF, λ, nm ( $\epsilon$ , M<sup>-1</sup> cm<sup>-1</sup>): 417 (34213), 299 (18471).

**[Zn<sup>II</sup>L<sup>1</sup>]<sub>2</sub>.** To H<sub>2</sub>L (0.11 g, 0.25 mmol) in chloroform (1 mL) was added Zn(CH<sub>3</sub>COO)<sub>2</sub>·2H<sub>2</sub>O (0.06 g, 0.25 mmol) in methanol (6 mL). After 24 h the crystals formed were filtered off, washed with methanol, and dried in air. Yield: 0.04 g, 36.0%. Calcd for C<sub>40</sub>H<sub>50</sub>ZnN<sub>6</sub>O<sub>6</sub>S<sub>4</sub> ( $M_r$  967.96 g/mol), %: C, 49.68; H, 5.22; N, 8.70; S, 13.24. Found, %: C, 49.24; H, 5.43; N, 8.42; S, 13.09. <sup>1</sup>H NMR (500.32 MHz, DMSO-*d*<sub>6</sub>): δ = 8.59 (s, 1H, CH=N), 8.55 (s, 1H, =CH-N), 7.28 (d, 1H, Ar), 7.11 (s, 1H, Ar), 7.06 (s, 1H, Ar), 2.56 (s, 3H, CH<sub>3</sub>), 2.51 (s, 3H, CH<sub>3</sub>), 2.34 (s, 3H, CH<sub>3</sub>), 2.33 (s, 3H, SCH<sub>3</sub>), 1.29 (s, 9H, C(CH<sub>3</sub>)<sub>3</sub>). ESI-MS (CH<sub>3</sub>OH) positive: m/z 486 [ZnL +

H]<sup>+</sup>, 506 [ZnL + Na]<sup>+</sup>, 522 [ZnL + K]<sup>+</sup>. IR spectrum, (ATR, selected bands,  $\nu_{\text{max}}$ ): 2964, 2914, 1593, 1470, 1372, 1288, 1249, 1167, 1022, 931, 825, 763, 612 cm<sup>-1</sup>. UV-vis in CHCl<sub>3</sub>, λ, nm ( $\epsilon$ , M<sup>-1</sup> cm<sup>-1</sup>): 431 (9279), 364 (20333), 314 (24601). The quality of the crystals was suitable for X-ray diffraction analysis.

**NiL<sup>2</sup>.** A mixture of 5-*tert*-butyl-2-hydroxy-3-phenylsulfanylbenzaldehyde S-methylisothiosemicarbazide (0.76 g, 2.1 mmol) and Ni(acac)<sub>2</sub> (0.51 g, 2.0 mmol) in pentane-2,4-dione (20 mL) and triethyl orthoformate (5 mL) were heated under argon atmosphere and stirring at 107 °C for 8 h. The isolated red precipitate washed with cold ethanol (5 mL), dissolved in dichloromethane (20 mL), filtered off, and evaporated to 1/3 of initial volume. Ethanol (15 mL) was added, and the red crystals formed were filtered off, washed with ethanol, and dried in vacuo. Yield: 0.27 g, 48.2%. Calcd for C<sub>25</sub>H<sub>27</sub>NiN<sub>3</sub>O<sub>3</sub>S<sub>2</sub>·0.7H<sub>2</sub>O ( $M_r$  552.94 g/mol), %: C, 54.30; H, 5.18; N, 7.60; S, 11.60. Found, %: C, 54.56; H, 4.91; N, 7.45; S, 11.14. ESI-MS (CH<sub>3</sub>OH) positive: m/z 540 [M + H]<sup>+</sup>, 562 [M + Na]<sup>+</sup>. <sup>1</sup>H NMR (500.32 MHz, CDCl<sub>3</sub>): δ 1.284 (s, 9H, C(CH<sub>3</sub>)<sub>3</sub>), 2.416 (s, 3H, SCH<sub>3</sub>), 2.637 (s, 3H, CH<sub>3</sub>), 2.711 (s, 3H, CH<sub>3</sub>), 7.128 (d, <sup>4</sup>J<sub>(H4-H6)</sub> = 2 Hz, 1H, Ar-H), 7.180 (d, <sup>4</sup>J<sub>(H4-H6)</sub> = 2 Hz, 1H, Ar-H), 7.340 (m, 3H, Ar-H), 7.523 (m, 1H, Ar-H), 7.537 (m, 1H, Ar-H), 7.896 (s, 1H, =CH-N), 8.118 (s, 1H, CH=N). UV-vis in CHCl<sub>3</sub>, λ, nm ( $\epsilon$ , M<sup>-1</sup> cm<sup>-1</sup>): 471 (6615), 382 (18750). X-ray diffraction quality single crystals were grown in an NMR tube by overlaying the solution of the complex in CH<sub>2</sub>Cl<sub>2</sub> with pentane.

**CuL<sup>2</sup>.** A mixture of 5-*tert*-butyl-2-hydroxy-3-phenylsulfanylbenzaldehyde S-methylisothiosemicarbazone (0.79 g, 2.1 mmol) and Cu(acac)<sub>2</sub> (0.55 g, 2.0 mmol) in pentane-2,4-dione (20 mL) and triethyl orthoformate (5 mL) were heated and stirred under argon atmosphere at 107 °C for 8 h. The brown precipitate was filtered off and evaporated to 1/3 of initial volume. Ethanol (15 mL) was added, and the brown crystals formed were filtered off, washed with ethanol, and dried in vacuo. The product was purified by column chromatography on silica by using CH<sub>2</sub>Cl<sub>2</sub> as an eluent. The fraction with the brown product was evaporated to dryness. Ethanol (15 mL) was added, and the precipitate was filtered off, washed with ethanol (5 mL), and dried in vacuo. Yield: 0.20 g, 18.4%. Calcd for C<sub>25</sub>H<sub>27</sub>CuN<sub>3</sub>O<sub>3</sub>S<sub>2</sub> ( $M_r$  545.18 g/mol), %: C, 55.08; H, 4.99; N, 7.71; S, 11.76. Found, %: C, 55.10; H, 5.03; N, 7.55; S, 11.46. ESI-MS (CH<sub>3</sub>OH) positive: m/z 483 [M + H]<sup>+</sup>, 505 [M + Na]<sup>+</sup>, 521 [M + K]<sup>+</sup>. IR spectrum, (ATR, selected bands,  $\nu_{\text{max}}$ ): 2961, 1660, 1586, 1510, 1464, 1429, 1364, 1290, 1165, 1120, 933, 781, 645 cm<sup>-1</sup>. UV-vis in CHCl<sub>3</sub>, λ, nm ( $\epsilon$ , M<sup>-1</sup> cm<sup>-1</sup>): 447 (10150), 377 (23880), 334 (21590).

**Oxidation of Primary Alcohol (Benzyl Alcohol) Using TEMPO/Air and TBHP.** The reactions were carried out in 20 mL round-bottom flasks equipped with condensers under atmospheric pressure of air. (i) TEMPO/air: Typically, to 5.0 mL of 1:1 (v/v) MeCN/0.1 M K<sub>2</sub>CO<sub>3</sub> aqueous solution were added 3.0 mmol of alcohol, 3 μmol (0.1 mol % vs substrate) of catalyst, and 0.15 mmol (5 mol % vs substrate) of TEMPO. (ii) TBHP: To 5.0 mL of 1:1 (v/v) MeCN/0.1 M K<sub>2</sub>CO<sub>3</sub> aqueous solution were added alcohol (3.0 mmol), catalyst (3 μmol), and TBHP (15 mmol). The reaction solutions in all cases were vigorously stirred using magnetic stirrers, and an oil bath was used to achieve the desired reaction temperature (50 °C). After the oxidation reaction (24 h), reaction mixtures were neutralized by 1 mol/L HCl and then extracted with 10 mL of EtOAc. The organic phase was used for chromatographic analyses using acetophenone as the internal standard. Negligible reactions were observed when the TEMPO, TBHP, or catalyst was not employed.

**Peroxidative Oxidation of Sec-Alcohols Using Microwave-Assisted Method.** In a typical experiment, an alcohol substrate (5.00 mmol), TBHP (10.0 mmol), and catalyst (5 μmol, 0.1 mol % vs substrate) were introduced to a cylindrical Pyrex tube, which was then placed in the focused microwave reactor. The reaction mixture was stirred under microwave irradiation (10 W power) for 240 min at 80 °C. After the reaction, the mixture was allowed to cool to ambient temperature. The reaction samples were taken up by 5 mL of acetonitrile with 300 μL of benzaldehyde (internal standard) and analyzed by gas chromatography.

## ASSOCIATED CONTENT

### Supporting Information

Cyclic voltammograms of CuL<sup>1</sup> and CuL<sup>2</sup> recorded at different scan rates for (Figure S1), spectroelectrochemistry of NiL<sup>1</sup> in CH<sub>2</sub>Cl<sub>2</sub> at room temperature (Figure S2), potential dependence of difference UV-vis spectra measured during electrochemical reduction of NiL<sup>1</sup> in CH<sub>2</sub>Cl<sub>2</sub> (Figure S3), EPR spectrum of initial solution of CuL<sup>2</sup> in dichloromethane/DMF at 100 K and in situ spectroelectrochemistry of CuL<sup>2</sup> in acetonitrile (0.1 M TBAPF<sub>6</sub>) (Figure S4), potential dependence of UV-vis-NIR spectra measured during electrochemical reduction of CuL<sup>2</sup> in acetonitrile (Figure S5), spin density for <sup>1</sup>[CuL<sup>2</sup>]<sup>+</sup> cation singlet (Figure S6), experimental X-band EPR spectrum of oxidized Ni<sup>II</sup>L with two different simulations (Figure S7), temperature-dependent EPR spectra of one-electron-oxidized NiL<sup>2</sup> and EPR spectrum of one-electron-oxidized NiL<sup>2</sup> at 110 K measured in extended sweep width (Figure S8), effect of the amount of catalyst on the total yield and TON in the peroxidative oxidation of 1-phenylethanol to acetophenone by copper complexes 2, 5, 7, and 9 (Figure S9), TD-DFT computed electron transitions for <sup>2</sup>[CuL<sup>2</sup>]<sup>0</sup>, <sup>1</sup>[CuL<sup>2</sup>]<sup>+</sup>, and <sup>2</sup>[NiL<sup>2</sup>]<sup>+</sup> (Table S1), corrected relative energy data of the optimized structures under study (Table S2), selected electron structure characteristics of neutral ML complexes and their monocations (Table S3), and calculated spin-squares  $\langle S^2 \rangle$  and energy data of the structures under study obtained using unrestricted formalism (Table S4). This material is available free of charge via the Internet at <http://pubs.acs.org>.

## AUTHOR INFORMATION

### Corresponding Author

\*E-mail: vladimir.arion@univie.ac.at (V.B.A.), peter.rapta@stuba.sk (P.R.), pombeiro@ust.pt (A.J.L.P.).

### Notes

The authors declare no competing financial interest.

## ACKNOWLEDGMENTS

The financial support of the Science and Technology Assistance Agency (Contract No. APVV-0202-10), Slovak Grant Agency VEGA (Contracts No. 1/0679/11, 1/0327/12, and 1/0289/12), Austrian Agency for International Cooperation in Education and Research (OEAD), European Regional Fund, Sectorial Operational Programme “Increase of Economic Competitiveness”, Priority Axis 2 (SOP IEC-A2-O2.1.2-2009-2, ID 570, COD SMIS-CSNR: 12473, Contract 129/2010-POLISILMET), Fundação para a Ciência e a Tecnologia (FCT), Portugal, and its PTDC/QUI-QUI/102150/2008, PTDC-EQU-EQU-122025-2010 and PEst-OE/QUI/UI0100/2011 projects, as well as Russian Ministry of Science and Education (State Contract No. 16.552.11.7008) is gratefully acknowledged. We also thank Alexander Roller for collecting the X-ray diffraction data and Dr. Lukas Bucinsky (SUT Bratislava) for valuable discussions and technical support.

## REFERENCES

- (1) Arion, V. B.; Rapta, P.; Telser, J.; Shova, S. S.; Breza, M.; Lušpaj, K.; Kožíšek, J. *Inorg. Chem.* **2011**, *50*, 2918–2931.
- (2) Ito, N.; Phillips, S. E. V.; Stevens, C.; Ogel, Z. B.; McPherson, M. J.; Keen, J. N.; Yadav, K. D. S.; Knowles, P. F. *Nature* **1991**, *350*, 87–90.
- (3) Ito, N.; Phillips, S. E. V.; Yadav, K. D. S.; Knowles, P. F. *J. Mol. Biol.* **1994**, *238*, 794–814.
- (4) Kersten, P. J. *Proc. Natl. Acad. Sci. U.S.A.* **1990**, *87*, 2936–2940.
- (5) Whittaker, M. M.; Kersten, P. J.; Nakamura, N.; Sanders-Loehr, J.; Schweizer, E. S.; Whittaker, J. W. *J. Biol. Chem.* **1996**, *271*, 681–687.
- (6) Bork, P.; Doolittle, R. F. *J. Mol. Biol.* **1994**, *236*, 1277–1282.
- (7) Itoh, S.; Takayama, S.; Arakawa, R.; Furuta, A.; Komatsu, M.; Ishida, S.; Takamuku, S.; Fukuzumi, S. *Inorg. Chem.* **1997**, *36*, 1407–1416.
- (8) Wang, Y.; DuBois, J. L.; Hedman, B.; Hodgson, K. O.; Stack, T. D. P. *Science* **1998**, *279*, 537–540.
- (9) Wang, Y.; Stack, T. D. P. *J. Am. Chem. Soc.* **1996**, *118*, 13097–13098.
- (10) Thomas, F. *Eur. J. Inorg. Chem.* **2007**, 2379–2404.
- (11) Berkessel, A.; Douisset, M.; Bulat, S.; Glaubitz, K. *Biol. Chem.* **2005**, *386*, 1035–1041.
- (12) Butsch, K.; Günther, T.; Klein, A.; Stirnat, K.; Berkessel, A.; Neudörfl, J. *Inorg. Chim. Acta* **2013**, *394*, 237–246.
- (13) Oriol, M.; Jarjayes, O.; Kanso, H.; Philouze, C.; Neese, F.; Thomas, F. *Angew. Chem., Int. Ed.* **2010**, *49*, 4989–4992.
- (14) Benisvy, L.; Blake, A. K.; Collison, D.; Davies, E. S.; Garner, C. D.; McInnes, E. J. L.; McMaster, J.; Whittaker, G.; Wilson, C. *Dalton Trans.* **2003**, 1975–1985.
- (15) Benisvy, L.; Bill, E.; Blake, A. J.; Collison, D.; Davies, E. S.; Garner, C. D.; McArdle, G.; McInnes, E. J. L.; McMaster, J.; Ross, S. H. K.; Wilson, C. *Dalton Trans.* **2006**, 258–267.
- (16) Gerbeleu, N. V.; Palanciu, S. C.; Simonov, Yu. A.; Dvorkin, A. A.; Bourosh, P. N.; Reetz, M. T.; Arion, V. B.; Tollner, K. *Polyhedron* **1995**, *14*, 521–527.
- (17) Gerbeleu, N. V.; Arion, V. B.; Burgess, J. *Template Synthesis of Macrocyclic Compounds*; Wiley-VCH: Weinheim, Germany, 1999.
- (18) (a) Figiel, P. J.; Sibaoui, A.; Ahmad, J. U.; Nieger, M.; Räisänen, M. T.; Leskelä, M.; Repo, T. *Adv. Synth. Catal.* **2009**, *351*, 2625–2632. (b) Ahmad, J. U.; Figiel, P. J.; Räisänen, M. T.; Leskelä, M.; Repo, T. *Appl. Catal., A* **2009**, *371*, 17–21. (c) Figiel, P. J.; Leskelä, M.; Repo, T. *Adv. Synth. Catal.* **2007**, *349*, 1173–1179. (d) Gamez, P.; Arends, I. W. C. E.; Sheldon, R. A.; Reedijk, J. *Adv. Synth. Catal.* **2004**, *346*, 805–811. (e) Sheldon, R. A.; Arends, I. W. C. E. *Adv. Synth. Catal.* **2004**, *346*, 1051–1071. (f) Gamez, P.; Arends, I. W. C. E.; Reedijk, J.; Sheldon, R. A. *Chem. Commun.* **2003**, 2414–2415. (g) Jazdzewski, B. A.; Tolman, W. B. *Coord. Chem. Rev.* **2000**, *200*–*202*, 633–685. (h) Michel, C.; Belanzoni, P.; Gamez, P.; Reedijk, J.; Baerends, E. J. *Inorg. Chem.* **2009**, *48*, 11909–11920. (i) Belanzoni, P.; Michel, C.; Baerends, E. J. *Inorg. Chem.* **2011**, *50*, 11896–11904.
- (19) (a) Dijksman, A.; Arends, I. W. C. E.; Sheldon, R. A. *Org. Biomol. Chem.* **2003**, *1*, 3232–3237. (b) Que, L.; Tolman, W. B. *Nature* **2008**, *455*, 333–340.
- (20) (a) Figiel, P. J.; Kopylovich, M. N.; Lasri, J.; Guedes da Silva, M. F. C.; Silva, J. J. R. F.; Pombeiro, A. J. L. *Chem. Commun.* **2010**, *46*, 2766–2768. (b) Figiel, P. J.; Kirillov, A. M.; Guedes da Silva, M. F. C.; Lasri, J.; Pombeiro, A. J. L. *Dalton Trans.* **2010**, *39*, 9879–9888. (c) Kopylovich, M. N.; Mahmudov, K. T.; Guedes da Silva, M. F. C.; Kuznetsov, M. L.; Figiel, P. J.; Karabach, Y. Y.; Luzyanin, K. V.; Pombeiro, A. J. L. *Inorg. Chem.* **2011**, *50*, 918–931. (d) Kopylovich, M. N.; Karabach, Y. Y.; Guedes da Silva, M. F. C.; Figiel, P. J.; Lasri, J.; Pombeiro, A. J. L. *Chem.—Eur. J.* **2012**, *18*, 899–914.
- (21) Simonov, Yu. A.; Gerbeleu, N. V.; Bourosh, P. N.; Arion, V. B.; Revenko, M. D.; Pakhopol, V. S.; Malinowsky, T. I. *Dokl. Akad. Nauk SSSR* **1987**, *297*, 608–612.
- (22) Gerbeleu, N. V.; Simonov, Yu. A.; Revenko, M. D.; Arion, V. B.; Pakhopol, V. S.; Bourosh, P. N.; Indrichan, K. M.; Palii, S. P. *Koord. Khim.* **1988**, *14*, 806–812.
- (23) Bourosh, P. N.; Simonov, Yu. A.; Arion, V. B.; Sobolev, A. N.; Gerbeleu, N. V.; Pakhopol, V. S. *Kristallografiya* **1989**, *34*, 637–641.
- (24) Gerbeleu, N. V.; Arion, V. B.; Simonov, Yu. A.; Bourosh, P. N.; Dvorkin, A. A.; Indrichan, K. M. *Russ. J. Inorg. Chem.* **1990**, *35*, 515–519.
- (25) Addison, A. W.; Rao, T. N.; Reedijk, J.; van Rijn, J.; Verschoor, G. C. *J. Chem. Soc., Dalton Trans.* **1984**, 1349–1356.

- (26) Reglinski, J.; Morris, S.; Stevenson, D. E. *Polyhedron* **2002**, *21*, 2175–2182.
- (27) Singer, A. L.; Atwood, D. A. *Inorg. Chim. Acta* **1998**, *277*, 157–162.
- (28) Matalobos, J. S.; Garcíá-Deibe, A. M.; Fondo, M.; Navarro, D.; Bermejo, M. R. *Inorg. Chem. Commun.* **2004**, *7*, 311–314.
- (29) Müller, J.; Weyhermüller, T.; Bill, E.; Hildebrandt, P.; Ould-Moussa, L.; Glaser, T.; Wieghardt, K. *Angew. Chem., Int. Ed.* **1998**, *37*, 616–619.
- (30) Michel, F.; Torelli, S.; Thomas, F.; Duboc, C.; Philouze, C.; Belle, C.; Hamman, S.; Saint-Aman, E.; Pierre, J.-L. *Angew. Chem., Int. Ed.* **2005**, *44*, 438–441.
- (31) Halfen, J. A.; Young, V. G., Jr.; Tolman, W. B. *Angew. Chem., Int. Ed.* **1996**, *35*, 1687–1690.
- (32) Halfen, J. A.; Jazdzewski, B. A.; Mahapatra, S.; Berreau, L. M.; Wilkinson, E. C.; Que, L., Jr.; Tolman, W. B. *J. Am. Chem. Soc.* **1997**, *119*, 8217–8227.
- (33) Sokolowski, A.; Leutbecher, H.; Weyhermüller, T.; Schnepf, R.; Bothe, E.; Bill, E.; Hildebrandt, P.; Wieghardt, K. *J. Biol. Inorg. Chem.* **1997**, *2*, 444–453.
- (34) Zurita, D.; Gautier-Luneau, I.; Ménage, S.; Pierre, J.-L.; Saint-Aman, E. *J. Biol. Inorg. Chem.* **1997**, *2*, 46–55.
- (35) Jazdzewski, B. A.; Young, V. G., Jr.; Tolman, W. B. *Chem. Commun.* **1998**, 2521–2522.
- (36) Benisvy, L. A.; Blake, J.; Collison, D.; Davies, E. S.; Garner, C. D.; McInnes, E. J. L.; McMaster, J.; Whittaker, G.; Wilson, C. *Chem. Commun.* **2001**, 1824–1825.
- (37) Thomas, F.; Gellon, G.; Gautier-Luneau, I.; Saint-Aman, E.; Pierre, J.-L. *Angew. Chem., Int. Ed.* **2002**, *41*, 3047–3050.
- (38) Philibert, A.; Thomas, F.; Philouze, C.; Hamman, S.; Saint-Aman, E.; Pierre, J.-L. *Chem.—Eur. J.* **2003**, *9*, 3803–3812.
- (39) Laurent, A. D.; Jacquemin, D. *Int. J. Quantum Chem.* **2013**, DOI: 10.1002/qua.24438.
- (40) Rotthaus, O.; Thomas, F.; Jarjayes, O.; Philouze, C.; Saint-Aman, E.; Pierre, J.-L. *Chem.—Eur. J.* **2006**, *12*, 6953–6962.
- (41) Storr, T.; Wasinger, E. C.; Pratt, R. C.; Stack, T. D. P. *Angew. Chem., Int. Ed.* **2007**, *46*, 5198–5201.
- (42) Shimazaki, Y.; Stack, T. D. P.; Storr, T. *Inorg. Chem.* **2009**, *48*, 8383–8392.
- (43) Gore, E. S.; Busch, D. H. *Inorg. Chem.* **1973**, *12*, 1–3.
- (44) Wieghardt, K.; Walz, W.; Nuber, B.; Weiss, J.; Ozarowski, A.; Stratemeier, H.; Reinen, D. *Inorg. Chem.* **1986**, *25*, 1650–1654.
- (45) Jørgensen, C. *Coord. Chem. Rev.* **1966**, *1*, 164–178.
- (46) Chaudhuri, P.; Nazari Verani, C.; Bill, E.; Bothe, E.; Weyhermüller, T.; Wieghardt, K. *J. Am. Chem. Soc.* **2001**, *123*, 2213–2223.
- (47) Shimazaki, Y.; Yajima, T.; Tani, F.; Karasawa, S.; Fukui, K.; Naruta, Y.; Yamauchi, O. *J. Am. Chem. Soc.* **2007**, *129*, 2559–2568.
- (48) Knorr, R.; Hauer, H.; Weiss, A.; Polzer, H.; Ruf, F.; Löw, P.; Dvortsák, P.; Böhner, P. *Inorg. Chem.* **2007**, *46*, 8379–8390.
- (49) (a) Slaughter, L. M.; Collman, J. P.; Eberspacher, T. A.; Brauman, J. I. *Inorg. Chem.* **2004**, *43*, 5198–5204. (b) Di Nicola, C.; Karabach, Y. Y.; Kirillov, A. M.; Monari, M.; Pandolfo, L.; Pettinari, C.; Pompeiro, A. J. L. *Inorg. Chem.* **2007**, *46*, 221–230.
- (50) Rothenberg, G.; Feldberg, L.; Wiener, H.; Sasson, Y. *J. Chem. Soc., Perkin Trans.* **1998**, *2*, 2429–2434.
- (51) Semmelhack, M. F.; Schmid, C. R.; Cortes, D. A.; Chou, C. S. *J. Am. Chem. Soc.* **1984**, *106*, 3374–3376.
- (52) Cheng, L.; Wang, J.; Wang, M.; Wu, Z. *Inorg. Chem.* **2010**, *49*, 9392–9399.
- (53) (a) Dijksman, A.; González, A. M.; Payeras, A. M.; Arends, I.; Sheldon, R. A. *J. Am. Chem. Soc.* **2001**, *123*, 6826–6833. (b) Dijksman, A.; Arends, I. W. C. E.; Sheldon, R. A. *Chem. Commun.* **1999**, 1591–1592. (c) Lu, Z.; Ladrak, T.; Roubeau, O.; van der Toorn, J.; Teat, S. J.; Massera, C.; Gamez, P.; Reedijk, J. *Dalton Trans.* **2009**, 3559–3570. (d) Punta, C.; Gambarotti, C. *N-Hydroxy Derivatives: Key Organocatalysts for the Selective Free Radical Aerobic Oxidation of Organic Compounds*. In *Ideas in Chemistry and Molecular Sciences: Advances in Synthetic Chemistry*; Pignataro, B., Ed.; Wiley-VCH: Weinheim, 2010.
- (54) Whittaker, J. W. *Chem. Rev.* **2003**, *103*, 2347–2363.
- (55) Sylvestre, I.; Wolowska, J.; Kilner, C. A.; McInnes, E. J. L.; Halcrow, M. A. *Dalton Trans.* **2005**, 3241–3249.
- (56) Freund, M.; Paradies, T. *Ber. Dtsch. Chem. Ges.* **1901**, *34*, 3110–3122.
- (57) Rudolph, G.; Henry, M. C. *Inorg. Synth.* **1967**, *10*, 74–77.
- (58) SAINT-Plus (Version 7.06a) and APEX2; Bruker-Nonius AXS Inc.: Madison, WI, USA, 2004.
- (59) Sheldrick, G. M. *Acta Crystallogr., Sect. A* **2008**, *64*, 112–122.
- (60) Johnson, C. K.; Barnett, M. N. *ORTEP-3 for Windows*; Oak Ridge National Laboratory: 1998. Farrugia, L. J. *32-bit Implementation*; University of Glasgow: Glasgow, 1999.
- (61) Gaussian 03, Revision D.01. Frisch, M. J.; Trucks, G. W.; Schlegel, H. B.; Scuseria, G. E.; Robb, M. A.; Cheeseman, J. R.; Montgomery, J. A., Jr.; Vreven, T.; Kudin, K. N.; Burant, J. C.; Millam, J. M.; Iyengar, S. S.; Tomasi, J.; Barone, V.; Mennucci, B.; Cossi, M.; Scalmani, G.; Rega, N.; Petersson, G. A.; Nakatsuji, H.; Hada, M.; Ehara, M.; Toyota, K.; Fukuda, R.; Hasegawa, J.; Ishida, M.; Nakajima, T.; Honda, Y.; Kitao, O.; Nakai, H.; Klene, M.; Li, X.; Knox, J. E.; Hratchian, H. P.; Cross, J. B.; Adamo, C.; Jaramillo, J.; Gomperts, R.; Stratmann, R. E.; Yazyev, O.; Austin, A. J.; Cammi, R.; Pomelli, C.; Ochterski, J. W.; Ayala, P. Y.; Morokuma, K.; Voth, G. A.; Salvador, P.; Dannenberg, J. J.; Zakrzewski, V. G.; Dapprich, S.; Daniels, A. D.; Strain, M.-C.; Farkas, O.; Malick, D. K.; Rabuck, A. D.; Raghavachari, K.; Foresman, J. B.; Ortiz, J. V.; Cui, Q.; Baboul, A. G.; Clifford, S.; Cioslowski, J.; Stefanov, B. B.; Liu, G.; Liashenko, A.; Piskorz, P.; Komaromi, I.; Martin, R. L.; Fox, D. J.; Keith, T.; Al-Laham, M. A.; Peng, C. Y.; Nakaryakkara, A.; Chalacombe, M.; Gill, P. M. W.; Johnson, B.; Chen, W.; Wong, M. W.; Gonzales, C.; Pople, J. A. *Gaussian03, Revision C.02*; Gaussian, Inc.: Wallingford, CT, 2004.
- (62) Bachler, V.; Olbrich, G.; Neese, F.; Wieghardt, K. *Inorg. Chem.* **2002**, *42*, 4179–4193.
- (63) Yamaguchi, K.; Tsunekawa, T.; Toyoda, Y.; Fueno, T. *Chem. Phys. Lett.* **1988**, *143*, 371–376.